DESIGN AND SIMULATION OF A BORON-LOADED NEUTRON SPECTROMETER

A Thesis

by

THOMAS MICHAEL MARTIN

Submitted to the Office of Graduate Studies of
Texas A&M University
in partial fulfillment of the requirements for the degree of

MASTER OF SCIENCE

August 2012

Major Subject: Health Physics

Design and Simulation of a Novel Boron-loaded Neutron Spectrometer

DESIGN AND SIMULATION OF A BORON-LOADED NEUTRON SPECTROMETER

A Thesis

by

THOMAS MICHAEL MARTIN

Submitted to the Office of Graduate Studies of
Texas A&M University
in partial fulfillment of the requirements for the degree of

MASTER OF SCIENCE

Approved by:

Chair of Committee,	Stephen Guetersloh
Committee Members,	Leslie Braby
	Michael Speed
Head of Department,	Yassin Hassan

August 2012

Major Subject: Health Physics

ABSTRACT

Design and Simulation of a Boron-loaded Neutron Spectrometer.

(August 2012)

Thomas Michael Martin, B.S., Texas A&M University

Chair of Advisory Committee: Dr. Stephen Guetersloh

The measurement of the distribution of kinetic energy carried by neutron particles is of interest to the health physics and radiation protection industry. Neutron particle spectral fluence is essential to the calculation of absorbed dose, equivalent dose, and other dosimetric quantities . Current methods of neutron spectrometry require either a large number of individual measurements and *a priori* spectral information, or complex and delicate equipment. To reduce these deficiencies, a novel neutron spectrometer, consisting of plastic scintillating fibers in a hexagonal array, was simulated via Monte Carlo. Fiber size and boron content were varied to optimize response characteristics. The results were compared to industry standard multi-sphere spectrometers. Of the geometries and materials analyzed, it was found that smaller diameter fibers with 1% loading of natural boron provide the best efficiency and energy resolution. Energy resolution was found to be similar to multi-sphere spectrometers, with the ability to differentiate on the order of ten energy fluence groups. Near isotropic angular response was traded for significantly reduced detection time and increased simplicity. Spectral analysis of individual fiber response can provide directional

information based on the ratio of energy deposition by thermal neutrons to all neutrons. Future work using proton recoil spectral data from individual fibers will allow increases in energy resolution while reducing or eliminating the need for *a priori* spectral information.

ACKNOWLEDGEMENTS

I would like to thank my committee chair, Dr. Stephen Guetersloh, and my committee members, Dr. Leslie Braby and Dr. Michael Speed, for their guidance and support throughout the course of this research.

Thanks also go to my many good friends, both within the department and without. I would also like to thank both the faculty and staff of the Department of Nuclear Engineering and the Radiological Safety Staff at Texas A&M University.

Finally, thanks to my parents, John and Lynn Martin, for their support through my time at Texas A&M University, and to my wife, Kendra, for her patience, encouragement, and love.

NOMENCLATURE

Bq	Becquerel
Ci	Curie
eV	Electron Volt
Gy	Gray
LET	Linear Energy Transfer
RBE	Relative Biological Effectiveness

TABLE OF CONTENTS

Page

LIST OF FIGURES

Page

LIST OF TABLES

1. INTRODUCTION

The measurement of the distribution of kinetic energy carried by neutrons has been of scientific interest since the early 1930's, when experiments leading to the discovery of the neutron were first performed (Chadwick 1932; Brooks and Klein 2002). The importance of this measurement has become more vital with widespread industrial and academic use of neutrons in the modern world. Fundamental physics and biological research, applied science, production of thermal and electrical power, medical therapy, nuclear forensics, and radiation protection are just a few of the more prominent fields in which knowledge of the neutron particle spectral fluence is essential (Nanstad et al. 1988; Tosi et al. 1991; Brooks and Klein 2002; Yan et al. 2002; Moody et al. 2005; Thomas 2010). The probability of a neutron interacting with matter, and given that an interaction occurs, the probability of a neutron undergoing a specific interaction, are highly dependent upon both the neutron kinetic energy and the composition and thermal energy of the target medium (Duderstadt and Hamilton 1976). Average quantities derived from these probabilities, or cross sections, such as kerma and absorbed dose, are therefore highly dependent upon the distribution of kinetic energy present in the incident neutron field (Caswell et al. 1980; Chadwick et al. 1999; Attix 2004). As can be seen in Table 1, neutron kerma factors, F_n (rad cm^2 n^{-1}), can span more than 11 decades within common materials for the range of neutron energies in commonly encountered environments (Attix 2004).

This thesis follows the style of Health Physics.

Similarly, quantities regarding the biological response to neutron exposures at the cellular and tissue levels, such as relative biological effectiveness (RBE), stochastic risk coefficients, and radiation-weighting (w_R) and tissue-weighting (w_T) factors, are dependent upon neutron energy (International Commission on Radiological Protection 2007). Derived quantities based upon these values are likewise neutron energy dependent. Practical methods for the measurement of neutron particle spectral fluence, or neutron spectrometry, are therefore of great importance to both fundamental physics at the microscopic level and applied use in the macroscopic world (Klein 1997; Naismith and Siebert 1997; Knoll 2000).

Table 1. Neutron kerma factors are given in several materials for the range of neutron energies commonly encountered.

E_n (MeV)	Hydrogen	Boron	Carbon	Nitrogen	Oxygen
			(rad cm^2 n^{-1})		
2.53×10^{-8}	4.20×10^{-12}	1.59×10^{-06}	2.41×10^{-15}	7.85×10^{-10}	3.56×10^{-17}
1.10×10^{-7}	2.04×10^{-12}	7.70×10^{-07}	1.30×10^{-15}	3.80×10^{-10}	4.18×10^{-17}
1.10×10^{-6}	7.49×10^{-13}	2.43×10^{-07}	9.71×10^{-16}	1.20×10^{-10}	2.82×10^{-16}
1.10×10^{-5}	1.28×10^{-12}	7.68×10^{-08}	6.11×10^{-15}	3.80×10^{-11}	2.78×10^{-15}
1.10×10^{-4}	1.08×10^{-11}	2.42×10^{-08}	6.00×10^{-14}	1.21×10^{-11}	2.78×10^{-14}
1.10×10^{-3}	1.07×10^{-10}	7.56×10^{-09}	5.99×10^{-13}	4.64×10^{-12}	2.78×10^{-13}
1.10×10^{-2}	1.00×10^{-09}	2.37×10^{-09}	5.93×10^{-12}	8.26×10^{-12}	2.78×10^{-12}
1.10×10^{-1}	6.50×10^{-09}	8.78×10^{-10}	5.46×10^{-11}	4.07×10^{-11}	2.82×10^{-11}
$1.10\times10^{+0}$	2.13×10^{-08}	4.58×10^{-10}	2.90×10^{-10}	1.89×10^{-10}	3.90×10^{-10}
$1.10\times10^{+1}$	4.61×10^{-08}	1.52×10^{-09}	1.34×10^{-09}	1.66×10^{-09}	1.50×10^{-09}
$1.95\times10^{+1}$	4.69×10^{-08}	2.31×10^{-09}	3.67×10^{-09}	3.29×10^{-09}	2.62×10^{-09}

1.1 Radiological Calculations Utilizing Neutron Spectral Information

Several radiological values and calculations are dependent upon accurate knowledge of neutron energy. On a microscopic scale, the cross sections for various reactions are heavily energy dependent. These microscopic dependencies influence fundamental macroscopic quantities, such as kerma and absorbed dose. In addition to these physical values, the response of tissue to neutrons is dependent upon particle energy.

1.1.1 Kerma and Absorbed Dose

Neutrons, and other indirectly ionizing radiations, do not directly deposit their energy within a medium. In nuclear collisions, energy is transferred to charged particles or other neutral particles. The secondary neutral particles continue on to transfer energy via further nuclear reactions, whereas the charged particles deposit their energy within the target medium. To quantify the energy transferred by neutron radiation, and consequently, the energy lost by the neutron radiation, the non-stochastic quantity kerma is used. Kerma is given by

$$K = \int_{E=0}^{E_{max}} \varphi(E')F_n(E')dE \quad (1)$$

where K is the kerma in rad (100 rad = 1 J kg^{-1} = 1 Gy), $\varphi(E')$ is the neutron fluence as a function of energy in n cm^{-2} MeV^{-1}, and $F_n(E')$ is the neutron kerma factor in rad cm^2 n^{-1} (Attix 2004). Neutron kerma factors have been tabulated for a variety of materials and

neutron energies, some examples of which are provided in Table 1 (Chadwick et al. 1999; Attix 2004).

The amount of energy deposited by secondary charged particles within a specific volume is quantified by the absorbed dose. Under charged particle equilibrium conditions, the absorbed dose from a field of neutrons can be approximated by

$$D = K \tag{2}$$

where the units are in rad or Gy, as appropriate. Only collisional kerma is considered, as radiative loss is negligible for secondary particles produced by neutrons with energies below tens of MeV. This approximation does not hold at higher incident neutron energies when the radiative contribution of charged recoil particles is non-zero (Attix 2004).

1.1.2 Biological Quantities

More important in the field of radiological protection are biological quantities related to neutron energy spectra. The equivalent dose delivered to tissue is of importance, as it gives a measure of the possible damage delivered with respect to stochastic effects. Equivalent dose is defined by

$$H_T = \sum_R w_R D_{T,R} \tag{3}$$

where H_T is the equivalent dose to a tissue, T, in rem (100 rem = 1 Sv = 1 J kg^{-1}), w_R is the unit-less radiation weighting factor for radiation R, and $D_{T,R}$ is the absorbed dose to tissue T from radiation R, in rad or Gy, as appropriate (International Commission on Radiological Protection 2007). The radiation weighting factor is defined in part by the relative biological effectiveness (RBE) of the specific radiation. The RBE is defined as the dose of a particular type of radiation required to create a specific biological endpoint with respect to the dose delivered by 250 kV x-rays. For neutrons, w_R values are given in tabulated form as a function of energy in ICRP 60 recommendations, and as a continuous function of neutron energy in ICRP 103 recommendations (International Commission on Radiological Protection 1990; International Commission on Radiological Protection 2007). ICRP 60 weighting factors are provided in Table 2. ICRP 103 weighting factors are given by

$$w_R \begin{cases} = 2.5 + 18.2e^{-[\ln(E_n)]^2/6} & E_n < 1 \text{ MeV} \\ = 5.0 + 17.0e^{-[\ln(2E_n)]^2/6} & 1 \text{ MeV} \le E_n \le 50 \text{ MeV} \\ = 2.5 + 3.25e^{-[\ln(0.04E_n)]^2/6} & E_n > 50 \text{ MeV}. \end{cases} \quad (4)$$

The equivalent dose, as well as other radiological quantities of biological importance, such as committed equivalent dose and effective dose, are therefore highly dependent upon knowledge of the neutron spectral particle fluence. It follows that neutron spectrometers are essential for radiological protection work in environments where the

neutron field is significant (Drake and Bartlett 1997; Matzke et al. 1997; Naismith et al. 1997; Chadwick 1999; Zheng et al. 2008; Thomas 2010).

Table 2. ICRP 60 radiation weighting factors as a function of neutron energy.

E_n	w_R
E_n < 10 keV	5
10 keV≤ E_n ≤ 100 keV	10
100 keV < E_n ≤ 2 MeV	20
2 MeV < E_n ≤ 20 MeV	10
20 MeV < E_n	5

1.2 Methods of Neutron Spectrometry

Because of the indirectly ionizing nature of neutron radiation, detection methods are through interactions with other particles. Measurement of the effects of these interactions can allow calculation of the incident neutron energy distribution (Turner 2007). Many techniques of neutron spectral measurements have been developed over the years. These methods can be roughly grouped into four categories, based upon the physics and mechanisms involved. These detection methods are: measurement of recoil nuclei from neutron induced elastic scattering reactions; measurement of characteristic emissions from neutron interactions in targets with well-defined energy thresholds; unfolding techniques applied to an array of individual detectors or detector geometries, each with a unique response dependent upon neutron energy; and other methods, such as

time-of-flight and diffraction measurements (Brooks and Klein 2002; Thomas 2010). In more recent years, advances in materials and computing power have contributed to enhancement of these methods, either by the application of previously unfeasible techniques, or the combination of several of the above methods (Freeman et al. 1999; Grazioso et al. 1999; Mekherjee 2002). The mechanisms involved in neutron spectrometry are discussed in-depth below.

1.2.1 Recoil Nuclei

Recoil nuclei methods are based upon the measurement of energy and angular distributions of charged particles. These charged particles are singly or multiply charged nuclei undergoing recoil from neutron-induced elastic scattering reactions. The incident neutron energy may be deduced from simple kinematics at first approximation. Relativistic effects and higher order considerations must be introduced to achieve exact results (Ferrer et al. 1977; Attix 2004; Viviani et al. 2009). Recoil nuclei methods become impractical for neutron detection at energies below approximately 50 keV, due to both recoil physics and the need to discriminate against accompanying gamma radiation (Tsoulfanidis 1983; Pichenot et al. 2002).

Inelastic scattering reactions may also contribute to recoil nuclei. However, the correlation between recoil energy from inelastic scattering reactions and incident neutron energy is not direct. Inelastic scattering reactions are endothermic and have a minimum threshold energy corresponding to available excited states within the target nucleus. In general, threshold energies decrease with the number of available excited states within

the nucleus. For example, the threshold energy for inelastic scattering in uranium is on the order of tens of keV. Nuclei more suitable to spectrometric methods, with atomic number $Z \leq 10$, have thresholds on the order of MeV (National Nuclear Data Center 2011). The contribution of inelastic scattering reactions to recoil nuclei is therefore negligible at lower neutron energies in low Z materials. At higher neutron energies, up to approximately 15 MeV, the cross sections for inelastic-scattering reactions are negligible when compared to more important reactions. For neutron energies greater than approximately 15 MeV, nuclei recoil methods become impractical due to other effects, such as wall effects and non-linearities in detector response (Brooks and Klein 2002).

The energy transferred to recoil nuclei by elastic scattering of an incident neutron is approximately given by

$$E_R = E_n[1 - (1 + \alpha) - (1 - \alpha)\cos\omega] \tag{5}$$

where E_R is the recoil energy in MeV, E_n is the incident neutron energy in MeV, ω is the scattering angle in the center-of-mass reference frame, and α is given by

$$\alpha = \left(\frac{M-1}{M+1}\right)^2 \tag{6}$$

where M is the mass of the nucleus, in u. It is clear from the above equations that an incident neutron is capable of transferring essentially all of its kinetic energy via elastic scattering with hydrogen nuclei (M = 1). On average, the amount of neutron kinetic

energy transferred to the recoil hydrogen is one half E_n. Hydrogen recoil nuclei, or protons, are widely used in neutron spectrometry applications due to this efficient energy transfer, among other reasons. This also explains the efficacy of hydrogenous media in neutron moderation (Eichholz and Poston, 1982). At higher incident neutron energies, slightly heavier nuclei, such as carbon, nitrogen, or oxygen recoils, become important (Feather 1932). These elements, along with hydrogen, make up the majority of tissue; recoil detectors with similar atomic abundances as tissue may be used to simulate tissue response (Attix 2004). A more convenient formulation of eqn (5) is given by

$$E_R = E_n \frac{4M}{(1+M)^2} \cos^2 \theta \tag{7}$$

where θ is the scattering angle in the laboratory reference frame, given by

$$\theta = \frac{(\pi - \omega)}{2}. \tag{8}$$

As target mass increases, θ approaches ω.

Recoil nuclei detectors are of two general types, consisting of either recoil telescopes, in which a small range of recoil angles are measured with respect to incident neutrons, or volumetric detectors in which all recoil angles are measured. Recoil telescopes provide accurate information when either the incident neutron energy or angle is well defined. Consider elastic scattering in a two-dimensional plane, as seen in Fig. 1.

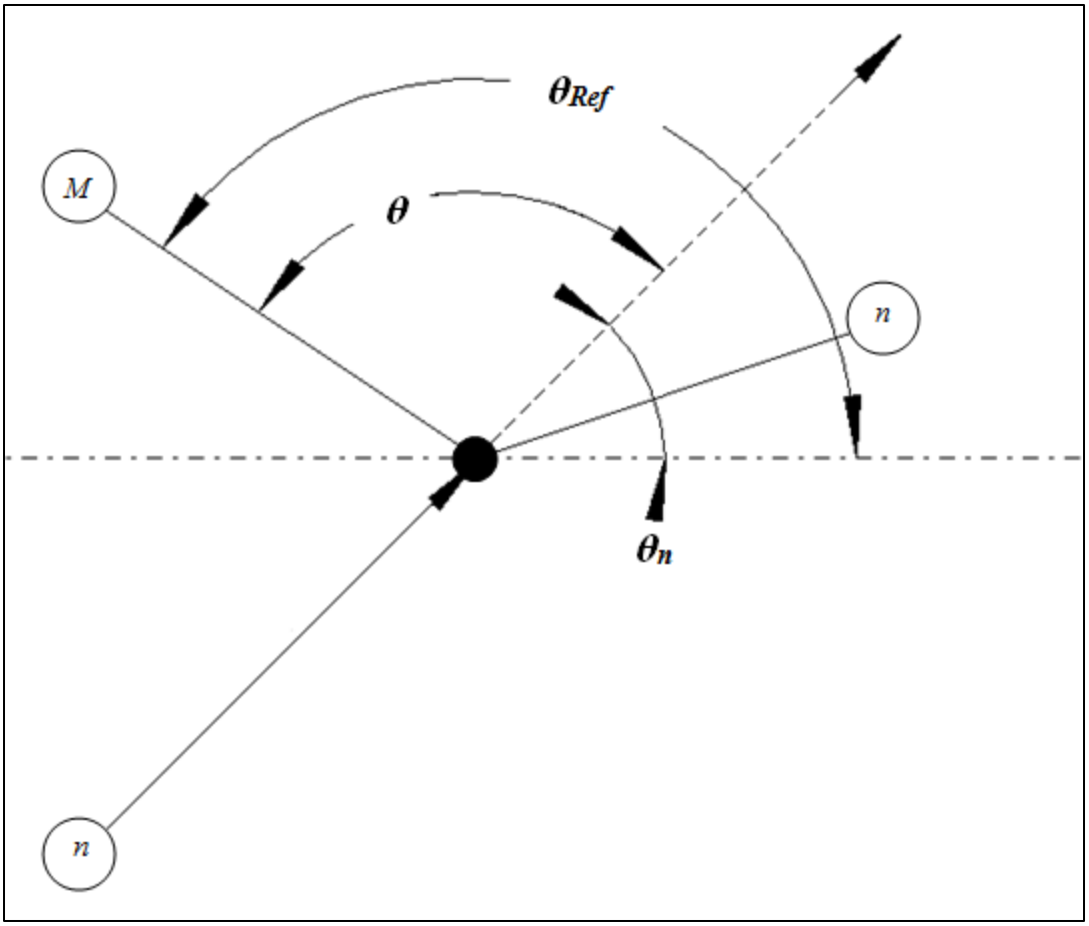

Fig. 1. Neutron-induced elastic scattering in two dimensions.

The incident neutron angle, with respect to the detector reference direction, is given by

$$\theta_n = \theta_{Ref} - \theta \tag{9}$$

where θ_n and θ_{Ref} are the incident neutron angle and the recoil angle with respect to the reference direction. Appropriate detector material will be able to measure the recoil

nuclei energy. By combination of eqns (7) and (9), the incident neutron energy and angle can be given in terms of the known quantities, as in eqn (10).

$$E_n \cos^2\left(\theta_{Ref} - \theta_n\right) = E_R \frac{(1+M)^2}{4M} \tag{10}$$

It is common to use such telescopes in cases where either the neutron beam direction or energy are well known, such that the remaining quantity can be solved. Note that the above equations are for the two-dimensional projection of a three-dimensional phenomenon. This works well when incident neutrons are at a small angle with respect to the detection plane, as shown in Fig. 1. Energy or angular resolution will necessarily decrease as the incident neutron angle relative to the detection plane increases (Singkarat et al. 1997; Titt et al. 1997; Peel et al. 2006; Tang et al. 2007).

Recoil telescopes consist of two or more detectors which measure events in coincidence. These may consist of a hexagonal or square array of plastic scintillating fibers, or one fixed and one (or more) movable detector arranged as shown in Fig 2.

Volumetric detectors, such as hydrogen-filled proton recoil proportional counters or organic scintillating detectors, measure recoil nuclei in all directions. The response functions for such detectors are broad continua, even when exposed to monoenergetic neutrons, such as from a deuteron-tritium neutron generator (Fowler and Brolley 1956; Brooks and Klein 2002; Zhang et al. 2003). The complex pulse height spectra of such detectors must be unfolded with cross section information to obtain interpretable response information (Pichenot et al. 2002; Thomas 2010). For organic scintillators, the

energy dependence of light yield must also be taken into account (Knoll 2000; Singkarat et al. 1993). Recoil nuclei that do not deposit all of their energy within the detector volume, i.e. those which are formed outside the detector sensitive volume and then enter, or those which form within the sensitive volume and escape, and multiple scattering events must also be taken into account.

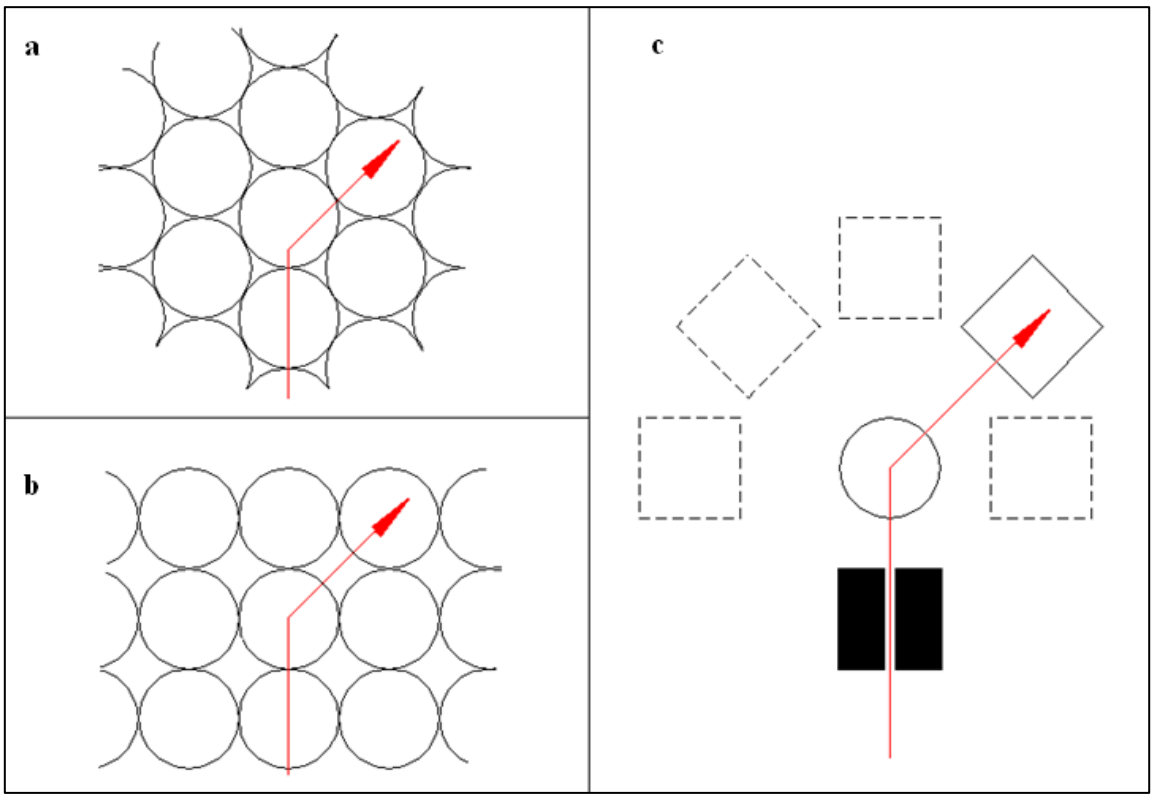

Fig. 2. Common recoil detection geometries. a) hexagonal array of scintillating fibers; b) square array of scintillating fibers; c) one fixed and one movable detector with a collimator.

A common method in use with volumetric plastic scintillators is to use capture gating techniques (Brooks and Klein 2002; Czirr et al. 2002). In capture gating techniques, detection occurs by measuring recoil nuclei from scatter reactions in coincidence with neutron capture. Neutron capture usually occurs after some short delay, on the order of microseconds. Many times, dopant materials are introduced into the scintillator volume. These materials have high thermal capture cross sections with characteristic emissions which are easily detected. Commonly used dopants are listed in Table 3 (Knoll 2000; Klykov et al. 2004; National Nuclear Data Center 2011). Because of the large capture cross-section of ^{10}B, natural boron, which is 19.95% abundant in ^{10}B, is the most common dopant used in conjunction with plastic scintillator material (Grazioso et al. 1999).

Table 3. Commonly used thermal capture nuclei.

Target Reaction	Capture Cross Section at 0.0253 eV (b)	Q-Value (keV)	Energy Distribution (keV)	
^{3}He (n, p) ^{3}H	5315.88	764	p ^{3}He	573 191
^{6}Li (n, ^{3}H) ^{4}He	954.651	4780	^{3}H ^{4}He	2730 2050
^{10}B (n, α) ^{7}Li	3842.45	2310[a]	α ^{7}Li	1470 840
^{157}Gd (n, γ) ^{158}Gd	253757	7940[b]	–	–

a. Li is emitted in the excited state (Q = 2.31 MeV) with a yield of 96%, which is accompanied by emission of a 482 keV gamma ray. 4% of the time Li is emitted in the ground state with Q = 2.792 MeV.

b. A wide range of gamma rays and conversion electrons are emitted in this reaction.

1.2.2 Threshold Reactions

Threshold reactions are based upon neutron capture reactions in various materials which result in characteristic emission. In general, these emissions are produced in radioactive decay of the neutron activation products, although in some cases prompt emission from the neutron reaction may be measurable. Radioactive product nuclei which emit gamma rays are convenient, as the incident neutron energy spectrum can be measured in real time via common gamma spectroscopy methods. A list of useful threshold nuclei is provided in Table 4 (Kuijpers et al. 1977; National Nuclear Data Center 2011). Note that ^{62}Cu decays primarily by positron emission; characteristic gamma rays are provided by annihilation reactions. It is clear that some radioisotopes, such as ^{24}Na, may be produced by multiple reactions, and that others, such as ^{115m}In and ^{196}Au, have emissions which would be difficult to differentiate. The list provided in Table 4 is by no means exhaustive, and it should be noted that the energy resolution of a detector based solely on threshold activation reactions would necessarily be coarse for these reasons. Except in specific applications, it is therefore common to use threshold activation methods in conjunction with other techniques (Kuijpers et al. 1977; International Atomic Energy Agency 2001; Thomas 2010). One such method is to use activation reactions in conjunction with a set of Bonner sphere detectors to increase the rank of the response matrix, as will be discussed in the next section (Routti and Sandberg 1985; Thomas et al. 2002; Vylet 2002).

Table 4. Useful threshold activation materials and their emissions.

Threshold Energy (MeV)	Reaction	Half-life	Gamma Energy (keV)	Gamma Abundance (Bq^{-1} s^{-1})
0.5	^{115}In (n, n') ^{115m}In	4.486 h	336.2	0.458
1.9	^{58}Ni (n, p) ^{58}Co	70.86 d	810.8	0.994
3.8	^{27}Al (n, p) ^{27}Mg	9.458 min	843.8 1015	0.718 0.282
4.9	^{27}Al (n, α) ^{24}Na	14.997 h	1369 2754	1.000 0.999
5.2	^{59}Co (n, α) ^{56}Mn	2.5789 h	846.8	0.988
6.0	^{24}Mn (n, p) ^{24}Na	14.997 h	1369 2754	1.000 0.999
8.6	^{197}Au (n, 2n) ^{196}Au	6.1669 d	333.0 355.7	0.229 0.870
9.3	^{127}I (n, 2n) ^{126}I	12.93 d	666.3	0.329
11.9	^{63}Cu (n, 2n) ^{62}Cu	9.673 min	511	1.950
13.0	^{58}Ni (n, 2n) ^{57}Ni	35.60 h	1378	0.817

1.2.3 Multisphere Detectors

Multisphere detectors, such as Bonner sphere systems and similar detectors, are capable of determining the neutron energy distribution by unfolding a set of detector measurements made with different detector geometries. Each geometry exhibits, ideally, a unique response at different neutron energies. The standard Bonner sphere system consists of a thermal neutron detector which may be surrounded by various thicknesses

of polyethylene or other moderating material. Each sphere thickness moderates neutrons by varying amounts. A response matrix can be constructed by calibrating the detector to a variety of neutron energies for each sphere size (Mares et al. 1991; Lacoste et al. 2004). The detector response when exposed to an unknown neutron energy distribution can be deconvoluted, or unfolded, to provide spectral information (Thomas and Alevra 2002; Esposito and Nandy 2004).

More formally, the neutron response is given by

$$M_i = \int R_i(E')\,\varphi(E')dE \tag{11}$$

where sphere i has a reading M_i in counts s^{-1}, $R_i(E')$ is the energy dependent response function of sphere i in cm^2, and $\varphi(E')$ is the neutron spectral fluence in n cm^{-2} s^{-1} MeV^{-1}. Eqn (11) is a Fredholm integral of the first kind, with no unique solution (Matzke 2002). Discretization of eqn (11) gives the approximation

$$M_i = \sum_{j=1}^{n} R_{ij}\varphi_j \tag{12}$$

where φ_j is the neutron fluence in energy group j, with energy bounds E_j and E_{j+1}, and R_{ij} is the analog of $R_i(E)$ averaged over energy group j. The set of $i=m$ equations and $j=n$ energy groups can be explicitly solved by numerical methods if $m \geq n$ (Twomey 1963). The total number of readings, m, is limited by the practical dimensions of the moderating spheres and the degree of uniqueness of each sphere's response. The uniqueness of the

set of sphere responses is given by the rank of the matrix $\boldsymbol{R}\cdot\boldsymbol{R}^{\boldsymbol{T}}$. As the number of spheres increases, so does the number of low-magnitude eigenvalues. An arbitrary cut-off value is chosen as a fraction of the principal eigenvalue; the number of eigenvalues greater than this cutoff, or rank, define the uniqueness of sphere responses. Uncertainties in response functions and measurements limit the system to at most n =10 to 20 well defined energy groups (Bramblett et al. 1960; Matzke 2002; Wiegel and Alevra 2002).

For commonly encountered neutron energy distributions, the energy resolution can be much higher than predicted by the rank method. In some operational use, such as for protection purposes within a nuclear power plant, the energy spectrum of the ambient neutron field changes little, i.e. the neutron energy spectrum can be routinely predicted (Klein 1997). The expected energy spectrum can be used with the sparse detector response information to fill the neutron energy fluence matrix. Many of the available unfolding programs incorporate large amounts of similar *a priori* spectral information. Correctly reconstructed neutron particle spectral fluence measurements depend then not only upon correct calibration information, but also the supplied estimates by the user regarding the expected spectra (Alevra et al. 1992; Garcia-Dominguez et al. 1999; El Messaoudi et. al; Cruzate et al. 2007).

The most common technique used in unfolding procedures is the least squares method, or minimization of the χ^2 term, given by

$$\chi^2 = \sum_{i=1}^{m} \left(\frac{M_i - M_{i,cal}}{S_i} \right) \tag{13}$$

where M_i is the measured reading given in eqn (8), and $M_{i,cal}$ is the calibration reading for sphere *i*. The uncertainty term, S_i, takes into account uncertainties in the measured readings, the response matrix, and *a priori* spectra information, if possible (Thomas et al. 1994; Thomas and Alevra 2002). Variations in unfolding methods, such as logarithmic least squares, entropy based algorithms, and others, have been used (Reginatto et al. 2002; Matzke 2002). In all cases, introduction of *a priori* information can introduce large and/or higher order uncertainty components in $\boldsymbol{S}$. Improper choice of *a priori* information can introduce non-real solutions, such as negative values within $\boldsymbol{\varphi}$, as well as other difficulties (Mares and Schraube 1994; Kralik et al. 1997; Matzke 2002). Genetic algorithms, which utilize an iterative process to determine "best fit" solutions, have been shown to provide somewhat satisfactory results without the use of *a priori* spectral information (Freeman et al. 1999; Mukherjee 2002).

In addition to inherent limits in energy resolution without *a priori* information, multisphere systems have the detriment of requiring several measurements. Ten to twelve measurements must be made, at a minimum of a few minutes each. Add to this the time required for switching moderating spheres, as well as unfolding analysis, and it is clear that a minimum of a few hours is required for measurement of the neutron energy spectrum at one position. However, there are many benefits with the use of multisphere systems. Gamma discrimination is easily achieved by ^{3}He and ^{10}B based thermal neutron detectors due to reaction Q-values. Multisphere systems exhibit near isotropic response. Furthermore, Bonner sphere systems have been in use since the early 1960's, and response functions for various geometries, materials, and common spectral

shapes are fairly well known for energies between approximately 10 keV and 20 MeV (Bramblett et al. 1960; Thomas and Alevra 2002). There is also a considerable amount of data for response functions of metal (lead, copper) lined multisphere systems at higher energies. These detectors rely on (n, xn) reactions within the metal to increase sensitivity at higher energies (Goldhagen et al. 2002; Wiegel and Alevra 2002). These detector sets are especially useful in accelerator facilities.

1.2.4 Other Methods

Several other methods have been used for the measurement of neutron spectral particle fluence. Some examples are time-of-flight measurements, neutron diffraction measurements, reflectometry, and neutron-slowing down spectrometry (Sawan and Conn 1974; Firk 1979; Loong et al. 1987; Karim et al. 1991; Telling and Andersen 2005). These methods have shown excellent results in the laboratory setting, but are not suited for operational radiation protection use due to complexity and/or fragility of the instruments used.

1.3 Focus of This Work

Neutron spectrometers currently in field use, particularly activation systems and multisphere systems, require extended measurement times, large volumes of equipment, or both. Recoil spectrometers require careful collimation, which may not be practical in operational use. An ideal neutron spectrometer for operational health physics use would provide high energy resolution with a small amount of equipment and relatively short

measurement times. Minimization of human interaction, such as the altering of detector geometry, is also preferable, as well is detector ruggedness. The goal of this study was to therefore develop and model a neutron spectrometer that incorporates as many of these characteristics as possible, while still remaining practical for operational use.

2. EXPERIMENTAL METHODS

2.1 Detector Design

General detector design consists of a hexagonal array of plastic, organic scintillating fibers. The various detector geometries and materials were simulated with the Monte Carlo neutron transport code MCNP5/X.

2.1.1 Geometry

Three different detector geometries were considered. Each detector consists of a bundle of fibers in a hexagonal array, with length equal to diameter, as measured across the points of the hexagon. A hexagonal array is depicted in Fig. 3, with dimensional parameters shown. Coordinate axes are shown to indicate direction. The origin is considered to be located at the center of the central fiber, at the midpoint of the fiber in the y-direction. Table 5 lists these parameters for each detector. Parameters include the number of fibers across the points of the array (*P)*, the number of fibers across the flats (*F*), the number of concentric "rings" (*i*), the total number of fibers (*N*), the fiber diameter (d_{fiber}), and the outer diameter (d_{outer}). It should be noted that d_{outer} remains fixed at 28.05 cm (11.04 in) for all three detector geometries. Approximate dimensions are quoted in inches. It is standard convention to denote the different spheres in Bonner sphere systems by their closest half-inch increments. The same notation has been adopted with this detector design to allow easy comparison between systems.

Ring diameters are provided in Table 6, both in actual diameter across the points in cm, and in approximate diameter, rounded to the nearest half-inch, in parenthesis. Indexing begins at the center. The inch notation or index will be used for future referencing of the rings.

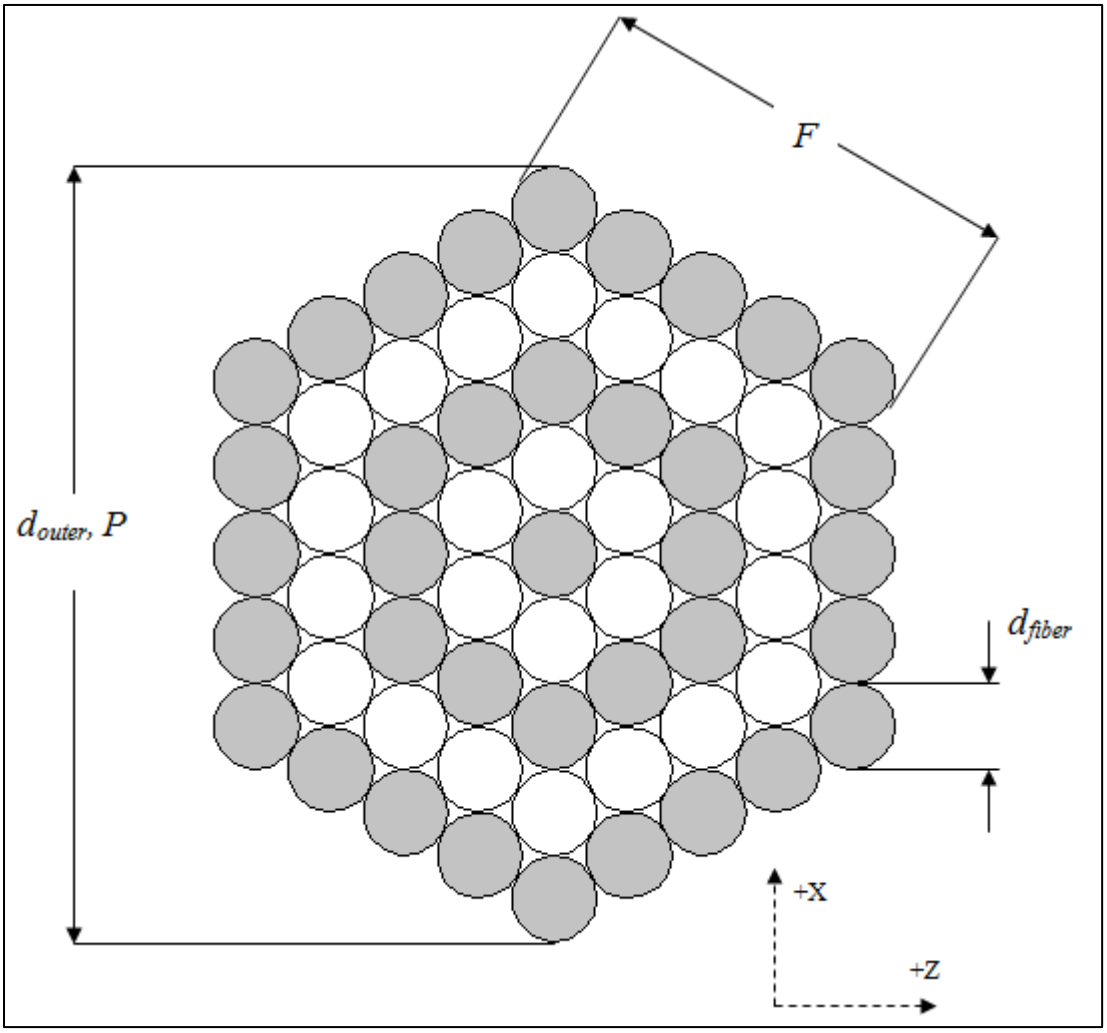

Fig. 3. Detector geometrical parameters.

Table 5. Geometrical parameters.

Parameter	Detector 1	Detector 2	Detector 3
Outer Diameter d_{outer}	28.05 cm (11 in)		
Fiber Diameter d_{fiber}	2.55 cm	1.87 cm	1.65 cm
Number of Fibers across Points P	11	15	17
Number of Fibers across Flats F	6	8	9
Number of Concentric Rings i	6	8	9
Total Number of Fibers N	91	169	217

Several considerations influenced the dimensions selected. A series of detectors with various d_{outer} values was considered. However, preliminary calculations suggested that the amount of moderation for smaller detector diameters was insufficient to provide a useful number of unique detector readings. Common Bonner sphere sets have maximum diameters on the order of 30 cm, or approximately one foot (Thomas and Alevra 2002). Thus similar overall dimensions were chosen for comparison purposes. Similarly, the number of sphere diameters in a standard multi-sphere set ranges between seven to ten. Fiber diameters were roughly selected to provide this number of concentric rings. The actual diameters chosen were selected because they provide the same overall detector dimension, d_{outer}, when arrayed as shown in Fig. 3.

Table 6. Ring diameters for each detector.

Ring Number (*i*)	Detector 1 "Large"	Detector 2 "Medium"	Detector 3 "Small"
1	2.55 cm (1")	1.87 cm (1")	1.65 cm (0.5")
2	7.65 cm (3")	5.61 cm (2")	4.95 cm (2")
3	12.75 cm (5")	9.35 cm (3.5")	8.25 cm (3")
4	17.85 cm (7")	13.09 cm (5")	11.55 cm (4.5")
5	22.95 cm (9")	16.83 cm (6.5")	14.85 cm (6")
6	28.05 cm (11")	20.57 cm (8")	18.15 cm (7")
7	–	24.31 cm (9.5")	21.45 cm (8.5")
8	–	28.05 cm (11")	24.75 cm (9.5")
9	–	–	28.05 cm (11")

2.1.2 Materials

Several material compositions were considered for the plastic scintillating fibers. It was desired to compare straight plastic scintillation material with various loadings of boron. Commercially available BC-408 and BC-454 were selected as the basis for the material specifications. This polyvinyl toluene (PVT) based material is readably available from Saint-Gobain (Saint-Gobain Crystals, 17900 Great Lakes Pkwy, Hiram, OH 44234, http://www.detectors.saint-gobain.com/). Material specifications taken from the Saint-Gobain BC-408 and BC-454 data sheets are supplied in Table 7. Boron loadings considered were 1%, 5%, and 10% natural boron by mass. This corresponds to

loadings of 0.1995%, 0.9975%, and 1.9950% ^{10}B by mass (Lide et al. 2005). In simulation, a density of 1.026 g cm^{-3} was used for BC-408 for consistency. For all materials, the MCNP material specification POLY.10t was used to accurately account for cross section variations due to hydrogen bonding in polymer at room temperature (Cruzate et al. 2007).

Table 7. BC-408 and BC-454 plastic scintillator properties.

Property	BC-408	BC-454		
% Boron, by mass	–	1%	5%	10%
% ^{10}B, by mass	–	0.1995%	0.9975%	1.9950%
Density (g cm^{-3})	1.032	1.026	1.026	1.026
Refractive Index	1.58	1.58	1.58	1.58
Light Output (% Anthracene)	64%	60%	48%	38%
Decay Time (ns)	2.1	2.2	2.2	2.2
Wavelength of Maximum Emission (nm)	425	425	425	425
Bulk Light Attenuation Length (cm)	380	120	120	120
H Atom Density (cm^{-3})	5.23×10^{22}	5.18×10^{22}	5.18×10^{22}	5.18×10^{22}
C Atom Density (cm^{-3})	4.74×10^{22}	4.63×10^{22}	4.43×10^{22}	4.18×10^{22}
^{10}B Atom Density (cm^{-3})	–	1.12×10^{20}	5.59×10^{20}	1.13×10^{21}
e^- Density (cm^{-3})	3.37×10^{23}	3.34×10^{23}	3.33×10^{23}	3.32×10^{23}

In actual detector construction, some means of preventing cross talk between fibers would need to be implemented. Standard methods involve vapor deposition of aluminum or some other material onto the exterior of the fibers (Blumenfeld et al. 1987). An interesting solution would be to coat the fibers with a plastic material of lesser refractive index to create an optical fiber with some degree of total internal reflection (Chakarova 1995). The small perturbation to array geometry and neutron interactions that these coatings would create were neglected in this study.

2.1.3 Electronics

Only basic signal collection and processing electronics were addressed in this study due to the simulation involved. Scintillation light collection could be achieved by the use of miniature silicon photomultipliers (Knoll 2000; Barbagallo et al. 2011). Silicon photomultipliers operate in avalanche mode and are capable of detecting extremely small signals, on the order of a few photons (Finocchiaro et al. 2008a; Finocchiaro et al. 2008b). Cross talk and dark current can be significant at low signals, so ideally a sensor should be placed at each end of each fiber to measure light pulses in coincidence (Finocchiaro et al. 2009). Silicon photomultipliers are available with active areas of 1 mm by 1 mm, as well as larger, so should be ideal for use with the fibers in this study (Barbagallo et al. 2011). For basic analysis, the total signal, with noise discrimination, from each fiber in a ring is summed. The total ring response can then be used with eqns (12) and (13) to solve for spectral energy fluence, with proper calibrations. More advanced processing may occur when multi-channel analyzers are connected with each fiber (Knoll 2000).

2.2 Neutron Sources

Several simulated neutron sources were used for determining detector characteristics. Monoenergetic neutron sources were used to estimate response functions for each detector. Each detector geometry and material combination was subjected to the EURADOS committee standard 47-group energy fluence (Freeman et al. 1999). This set uses 47 logarithmically equidistant energy points between 0.00793 eV and 19.95 MeV. Group number one corresponds to the highest energy by standard convention. The neutron energies used are provided in Table 8.

Table 8. EURADOS 47-group energy values.

Group	Energy (MeV)	Group	Energy (MeV)	Group	Energy (MeV)	Group	Energy (MeV)
1	2.00×10^{1}	13	7.04×10^{-2}	25	9.69×10^{-5}	37	8.77×10^{-7}
2	1.25×10^{1}	14	4.40×10^{-2}	26	6.06×10^{-5}	38	5.48×10^{-7}
3	7.78×10^{0}	15	2.75×10^{-2}	27	3.78×10^{-5}	39	3.42×10^{-7}
4	4.86×10^{0}	16	1.72×10^{-2}	28	2.36×10^{-5}	40	2.14×10^{-7}
5	3.04×10^{0}	17	1.07×10^{-2}	29	1.48×10^{-5}	41	1.33×10^{-7}
6	1.90×10^{0}	18	6.70×10^{-2}	30	9.22×10^{-6}	42	8.34×10^{-8}
7	1.19×10^{0}	19	4.18×10^{-3}	31	5.76×10^{-6}	43	5.21×10^{-8}
8	7.40×10^{-1}	20	2.61×10^{-3}	32	3.60×10^{-6}	44	3.25×10^{-8}
9	4.62×10^{-1}	21	1.63×10^{-3}	33	2.25×10^{-6}	45	2.03×10^{-8}
10	2.89×10^{-1}	22	1.02×10^{-3}	34	1.40×10^{-6}	46	1.27×10^{-8}
11	1.80×10^{-1}	23	6.37×10^{-4}	35	9.69×10^{-6}	47	7.93×10^{-9}
12	1.13×10^{-1}	24	3.98×10^{-4}	36	6.06×10^{-6}		

3. RESULTS AND DISCUSSION

3.1 Simulated Response

The normalized response functions for each detector geometry and configuration are shown in Figs. 4-15. Each ring response is shown on the same plot as a function of fiber size and material composition. Detector 1 (large fiber) response functions are shown in Figs. 4-7, for boron loadings of 0%, 1%, 5%, and 10%, respectively. Similarly, detector 2 (medium fiber) and detector 3 (small fiber) response functions are shown in Figs. 8-11 and Figs. 12-15, respectively. All response functions have been normalized to each other, so are shown in arbitrary units.

These response functions were found by simulating each detector iteration 47 times, corresponding to each discrete energy group listed in Table 8. The neutron beams were directed in the plus Z direction, normal to the hexagonal array, from a point outside of the detector volumes. The beams were centered on the detector longitudinal axis. The beam consisted of monodirectional particles, emitted from a distributed planar source with area equal to the cross sectional area of the detector.

3.2 Material Composition

Response functions for each material composition are plotted on the same chart for a few selected ring diameters of each detector in Figs. 16-25. A full set of these figures are provided in Appendix A. These figures show how detector efficiency changes with boron loadings. Pure plastic scintillator exhibited a significantly lower response

than the boron-loaded scintillators, except at the highest energies. The efficiency of 1% boron loaded fibers is greater than or equal to the efficiencies of other compositions for neutron energies below approximately 1 MeV. At energies above the 100 eV to 1 keV range, differences in response between the boron-loaded scintillators is negligible. The 1% boron loading provides increased sensitivity due to the thermal capture cross section, while providing the highest fraction of hydrogen for moderation. It is also clear that the fraction of moderated neutrons reaching the central fibers increases as the boron loading fraction decreases.

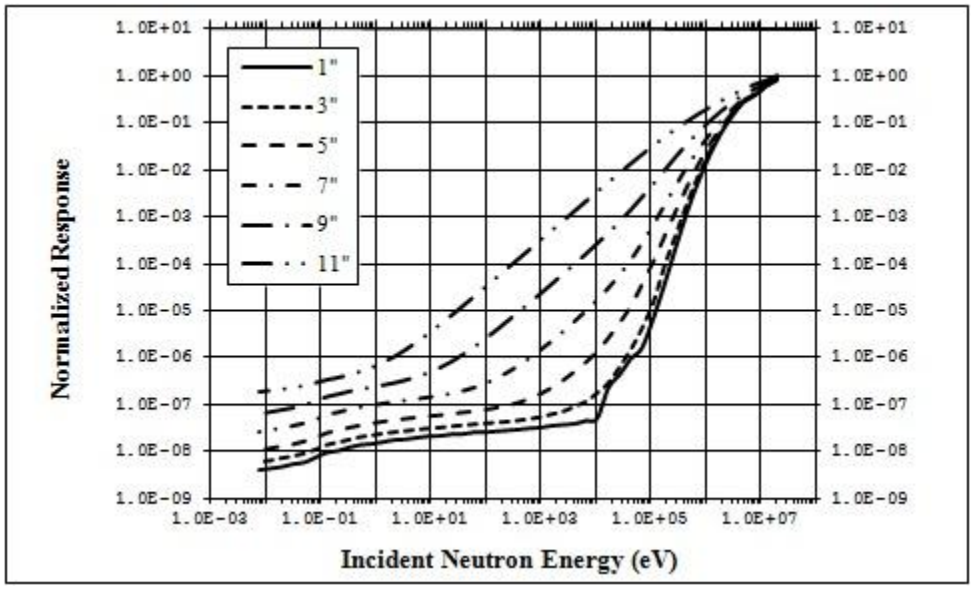

Fig. 4. Normalized detector 1 (large fiber) response functions are shown for 0% boron loading.

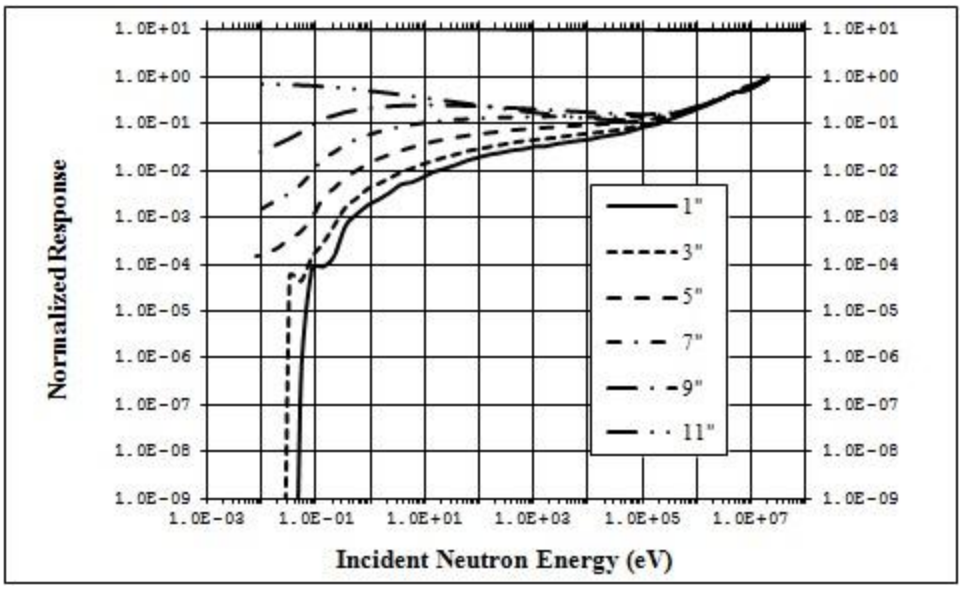

Fig. 5. Normalized detector 1 (large fiber) response functions are shown for 1% boron loading.

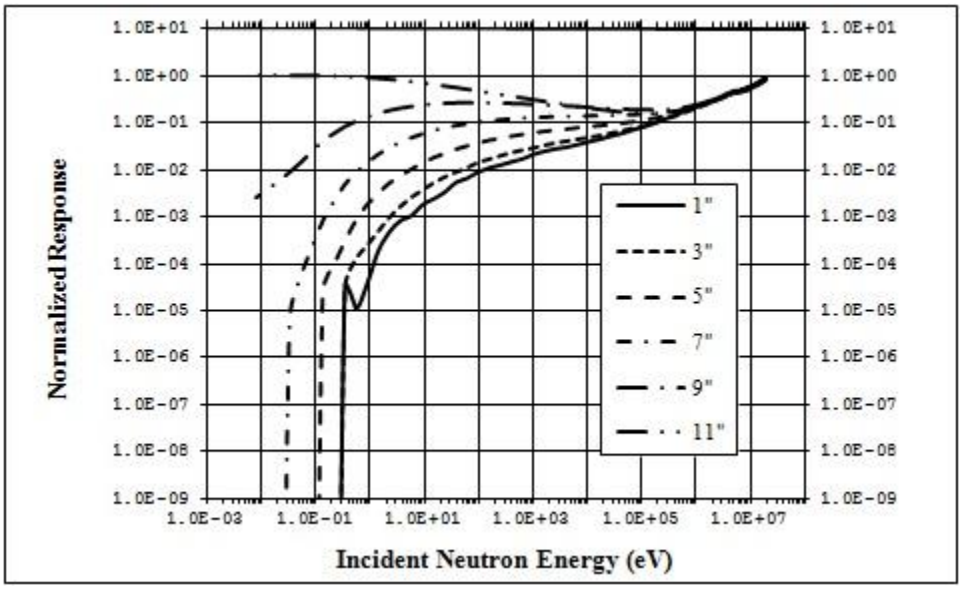

Fig. 6. Normalized detector 1 (large fiber) response functions are shown for 5% boron loading.

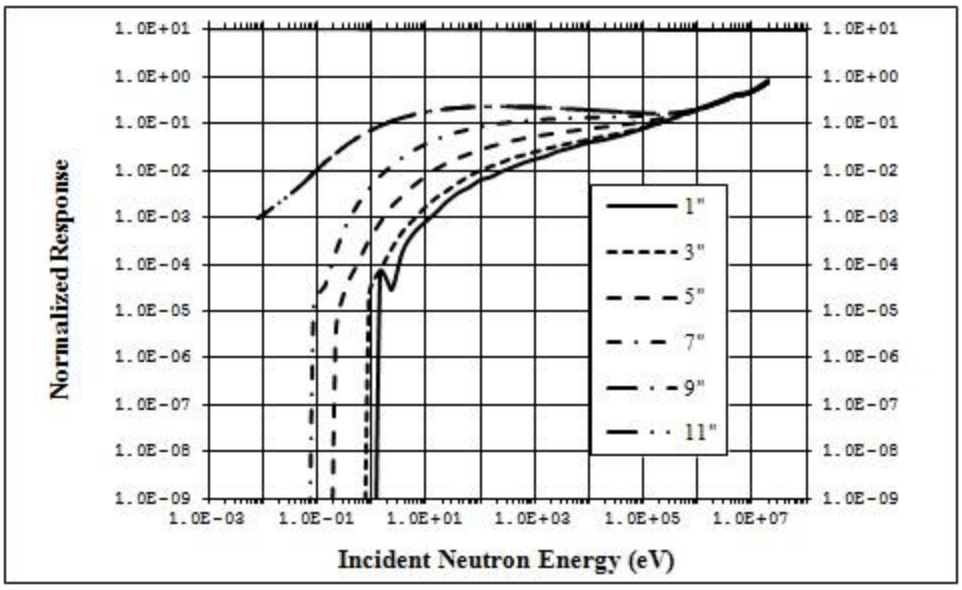

Fig. 7. Normalized detector 1 (large fiber) response functions are shown for 10% boron loading.

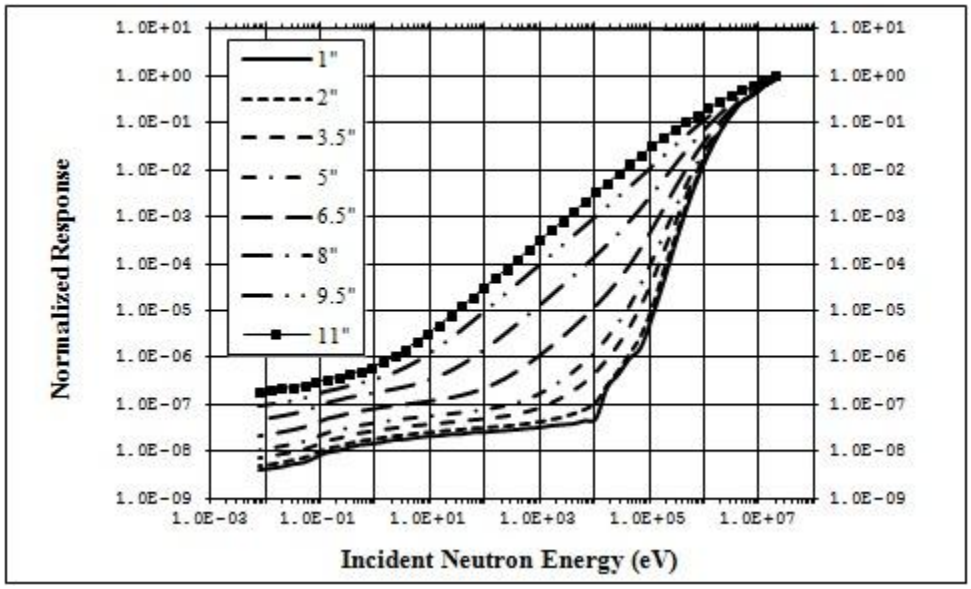

Fig. 8. Normalized detector 2 (medium fiber) response functions are shown for 0% boron loading.

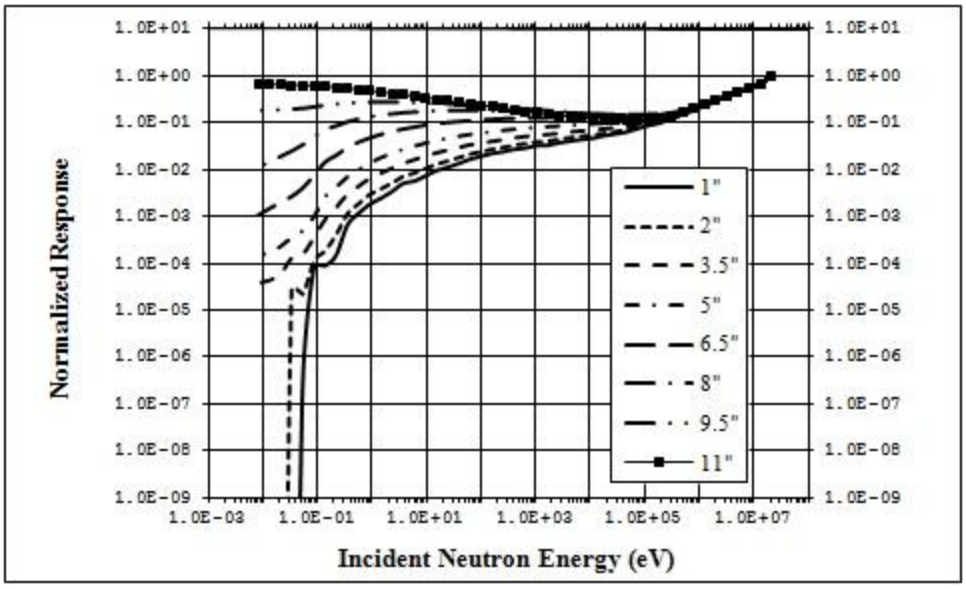

Fig. 9. Normalized detector 2 (medium fiber) response functions are shown for 1% boron loading.

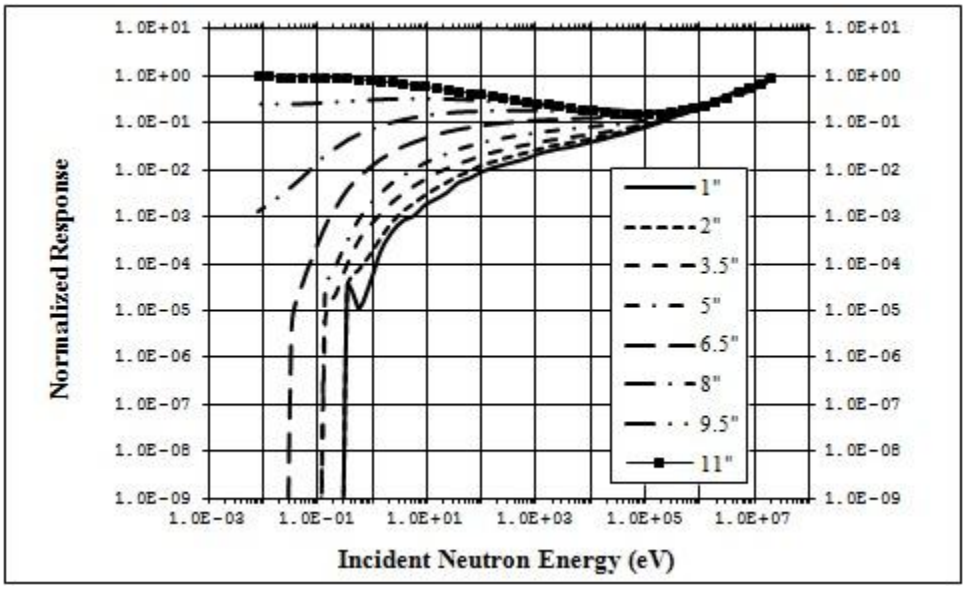

Fig. 10. Normalized detector 2 (medium fiber) response functions are shown for 5% boron loading.

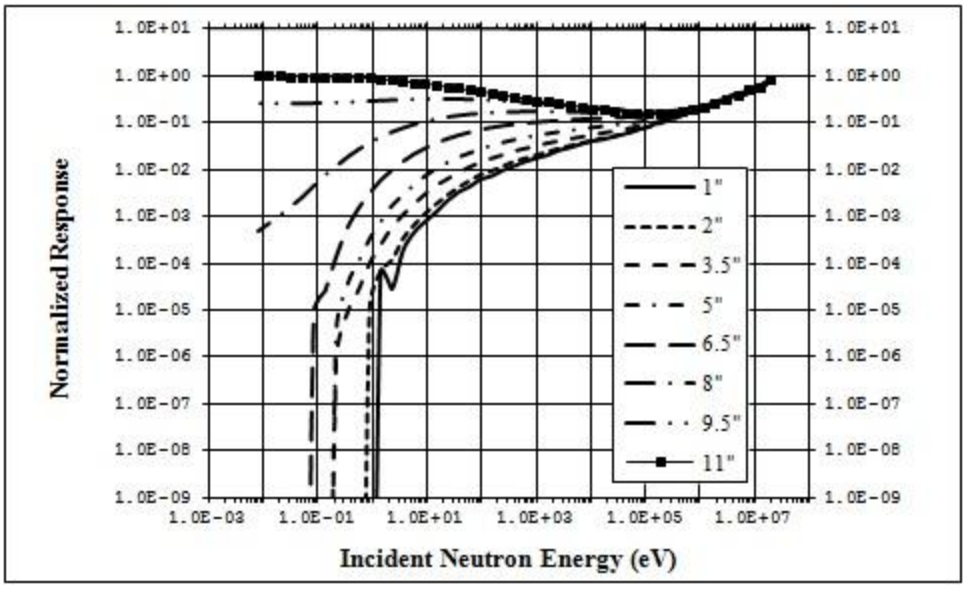

Fig. 11. Normalized detector 2 (medium fiber) response functions are shown for 10% boron loading.

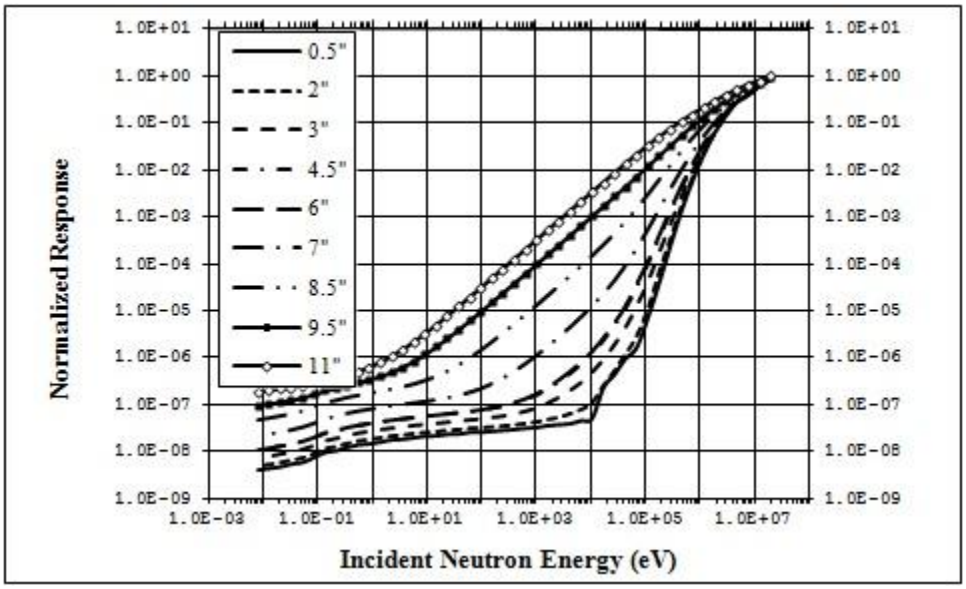

Fig. 12. Normalized detector 3 (small fiber) response functions are shown for 0% boron loading.

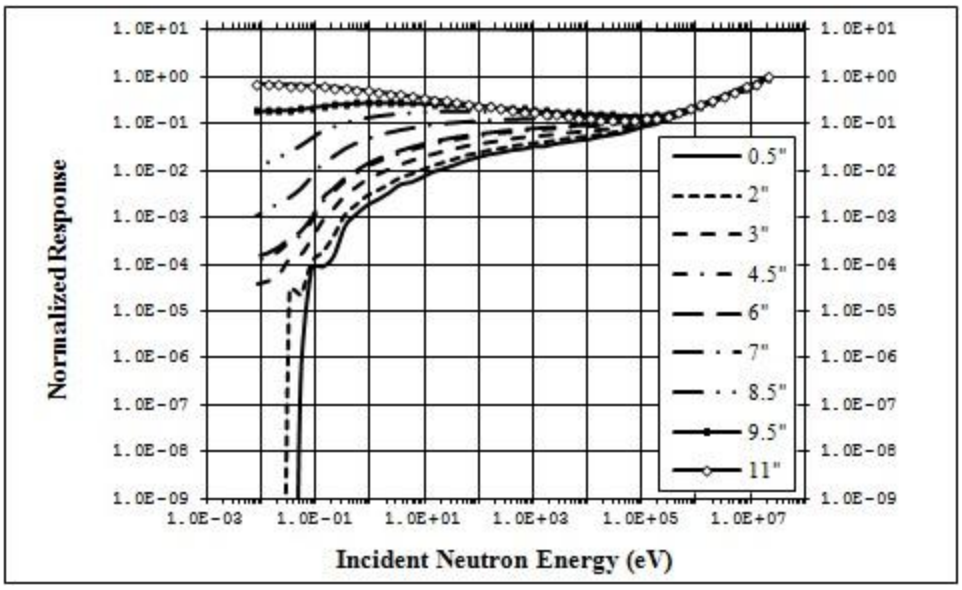

Fig. 13. Normalized detector 3 (small fiber) response functions are shown for 1% boron loading.

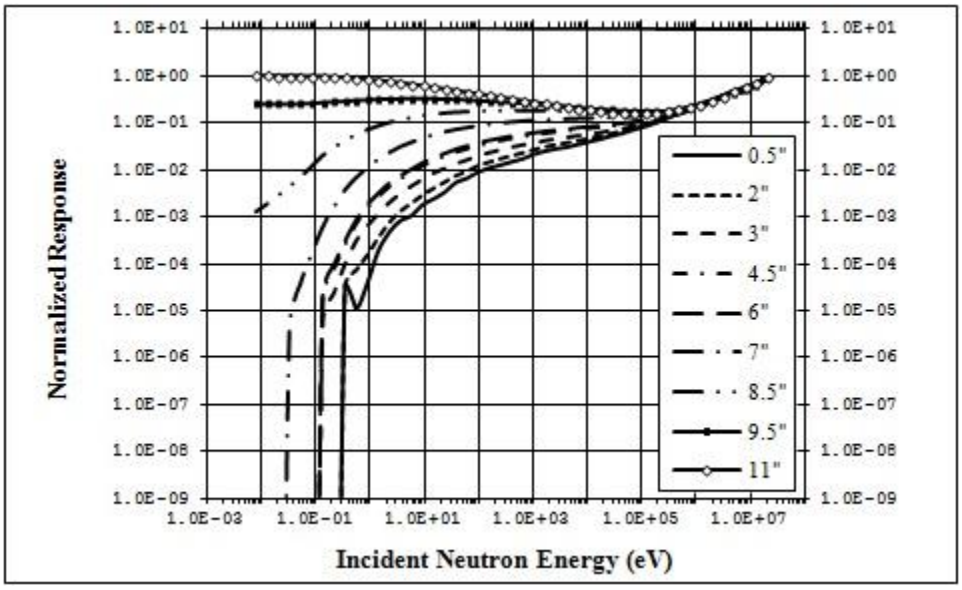

Fig. 14. Normalized detector 3 (small fiber) response functions are shown for 5% boron loading.

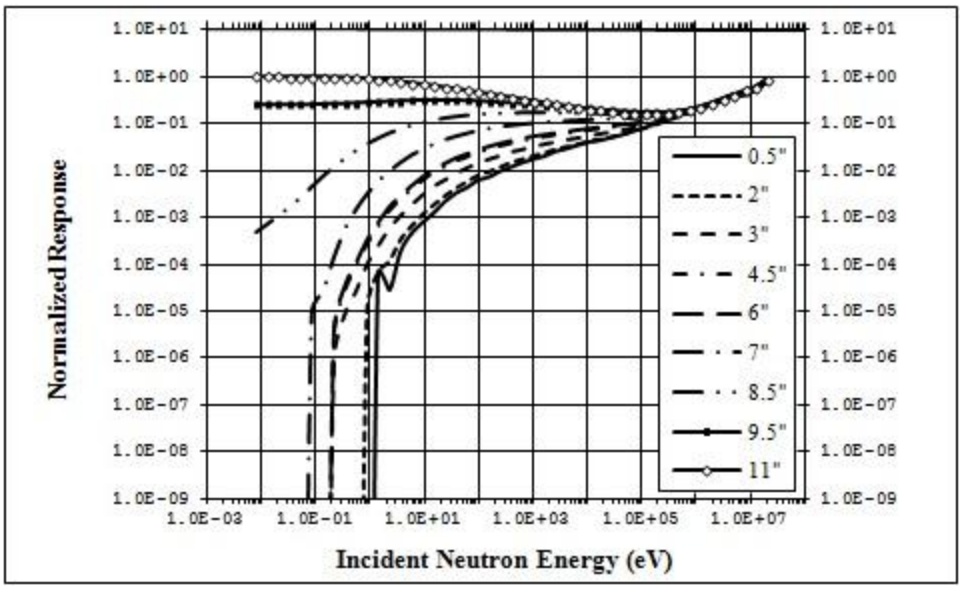

Fig. 15. Normalized detector 3 (small fiber) response functions are shown for 10% boron loading.

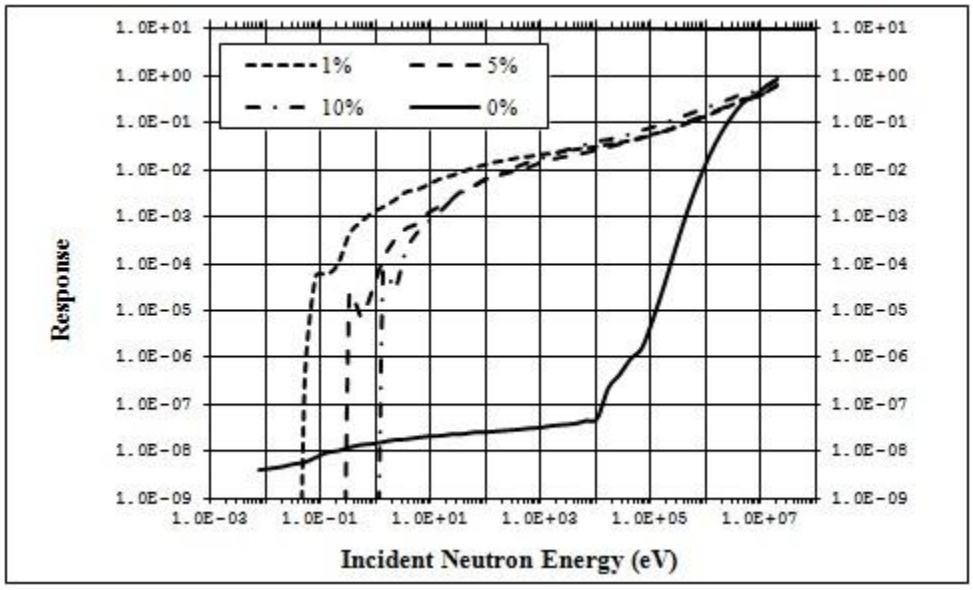

Fig. 16. Response functions are shown for the four material compositions for the 1" ring of detector 1 (large fiber).

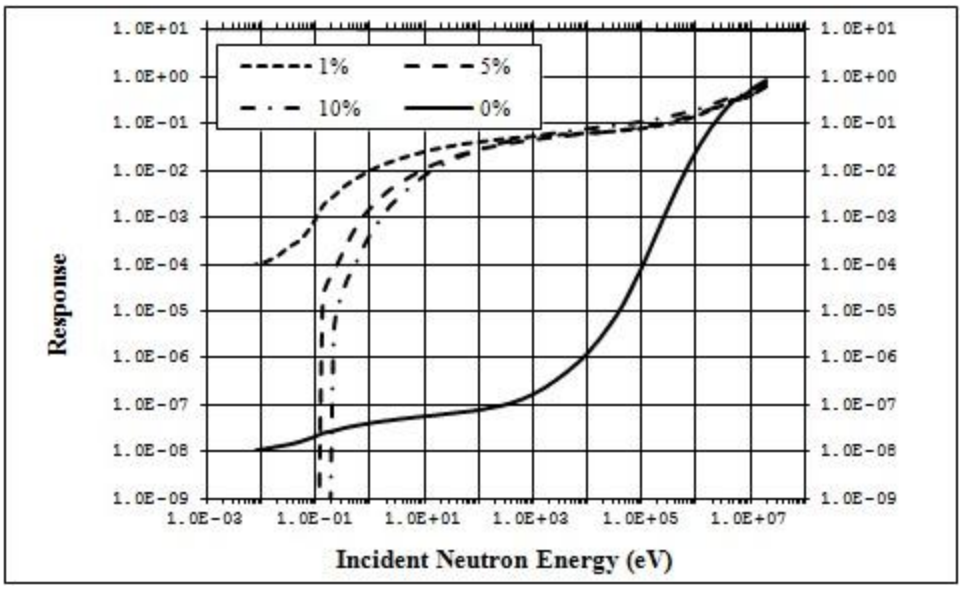

Fig. 17. Response functions are shown for the four material compositions for the 5" ring of detector 1 (large fiber).

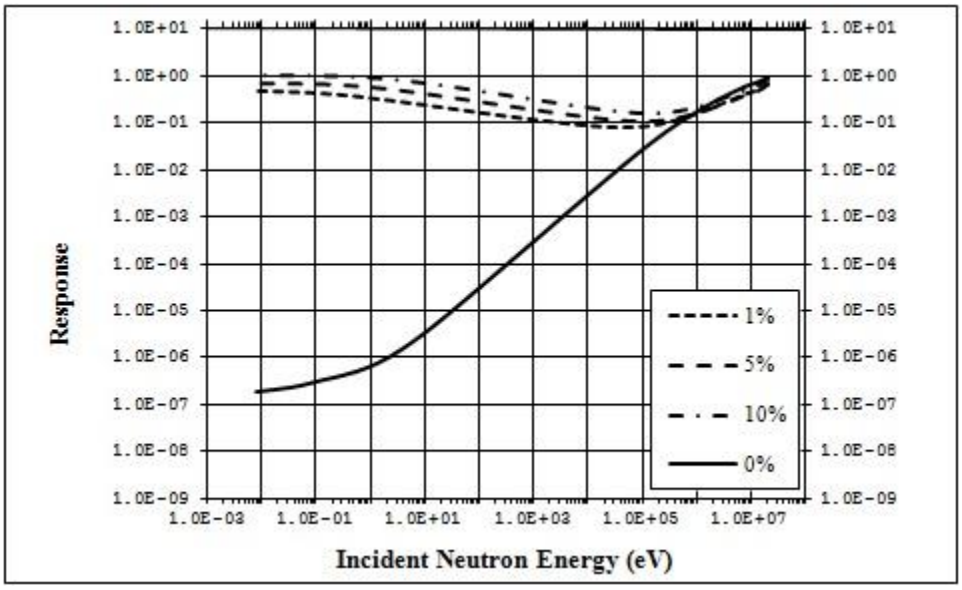

Fig. 18. Response functions are shown for the four material compositions for the 11" ring of detector 1 (large fiber).

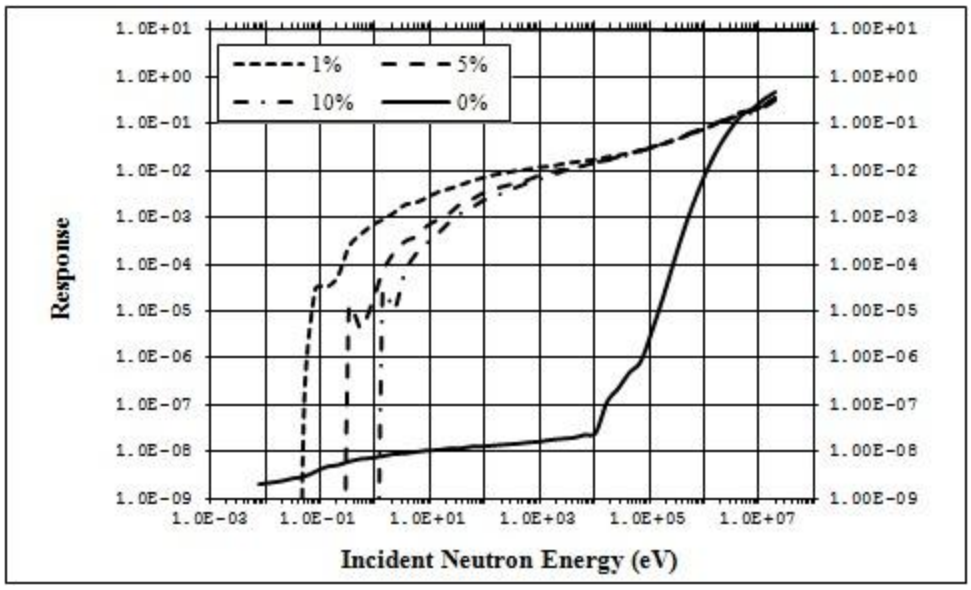

Fig. 19. Response functions are shown for the four material compositions for the 1" ring of detector 2 (medium fiber).

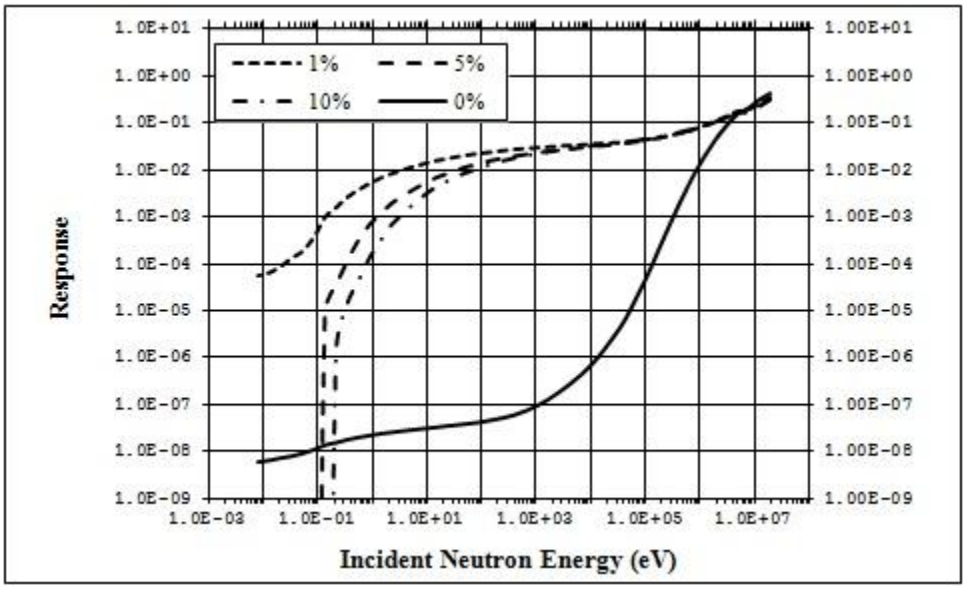

Fig. 20. Response functions are shown for the four material compositions for the 5" ring of detector 2 (medium fiber).

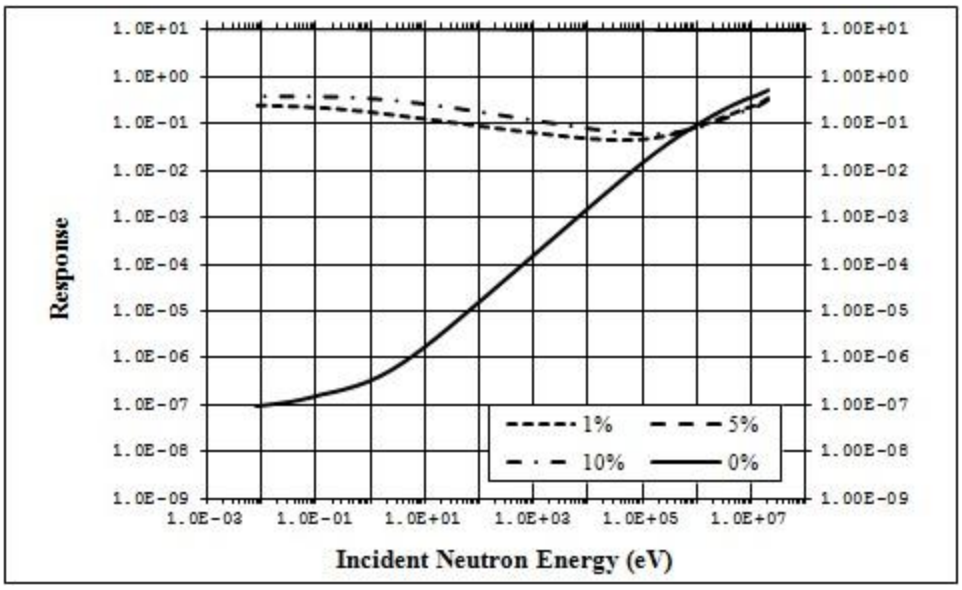

Fig. 21. Response functions are shown for the four material compositions for the 11" ring of detector 2 (medium fiber).

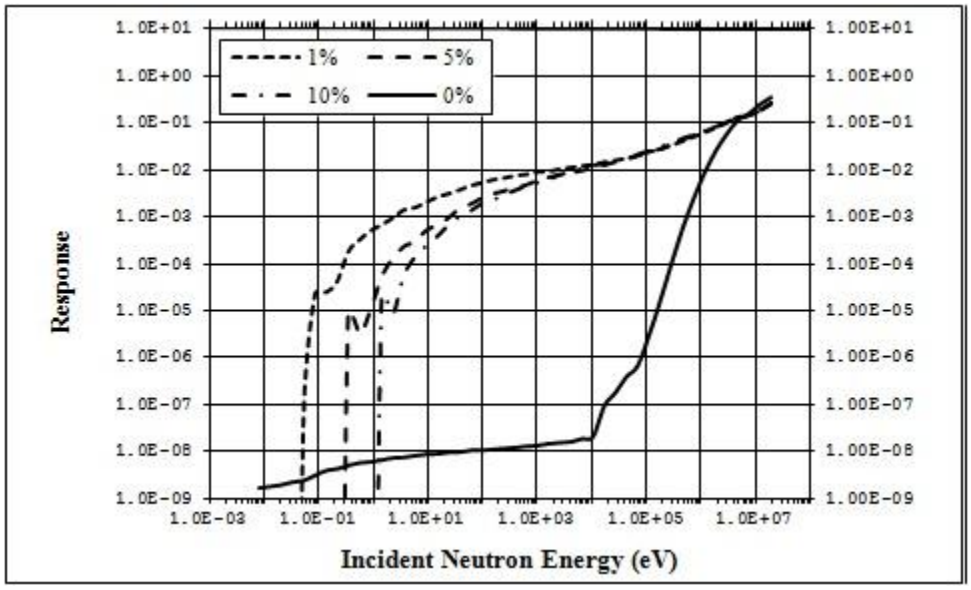

Fig. 22. Response functions are shown for the four material compositions for the 0.5" ring of detector 3 (small fiber).

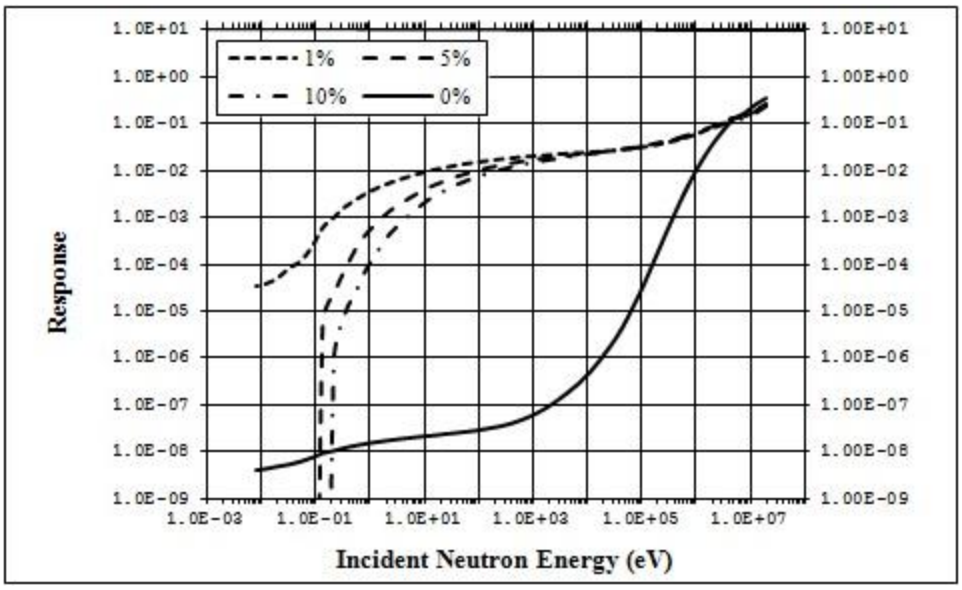

Fig. 23. Response functions are shown for the four material compositions for the 4.5" ring of detector 3 (small fiber).

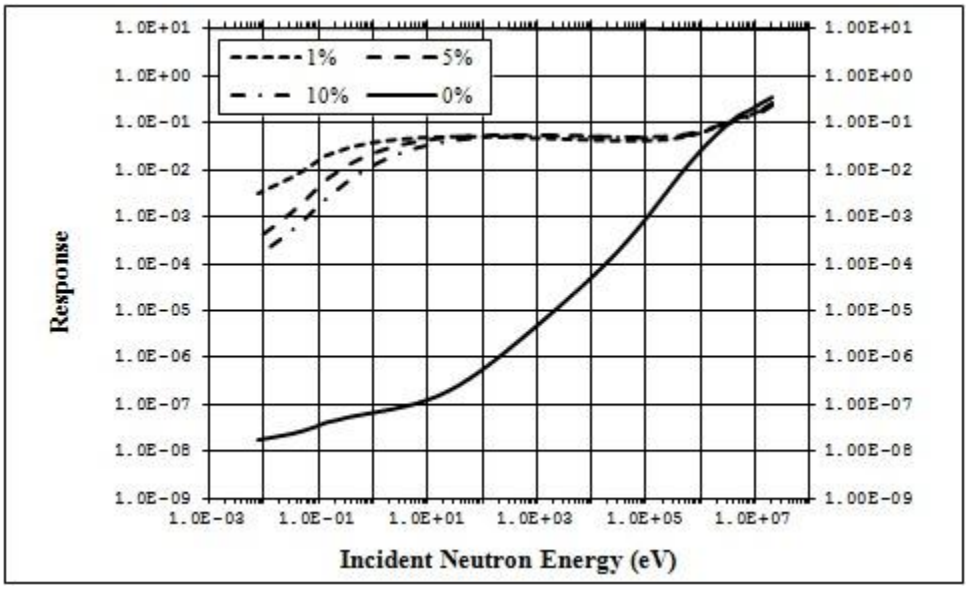

Fig. 24. Response functions are shown for the four material compositions for the 8.5" ring of detector 3 (small fiber).

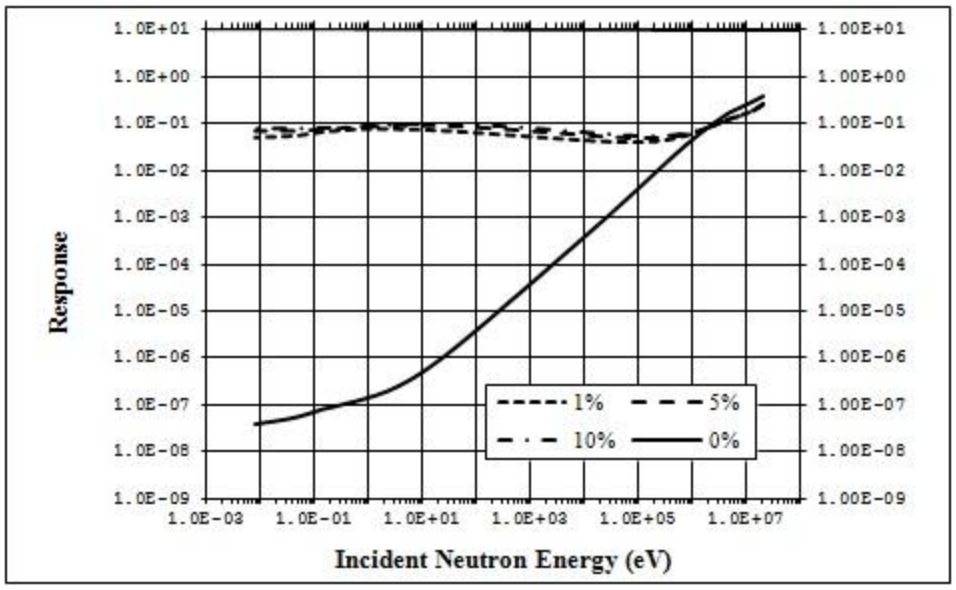

Fig. 25. Response functions are shown for the four material compositions for the 11" ring of detector 3 (small fiber).

3.3 Geometry

The relative response of each detector ring decreases as fiber diameter decreases. This seems most pronounced for the outermost rings. The response values at 19.95 MeV are given for the outer rings in Table 9. Relative response values are taken with respect to the 2.55 cm diameter fibers of similar composition. The relative response for each fiber size and composition is remarkably similar, which suggests a geometrical relationship.

Table 9. Outer ring (11”) response values at 19.95 MeV.

Detector	Material	Response	Relative Response
Detector 1 2.55 cm Fiber Diameter	PVT	0.944	1.000
	1% B	0.672	1.000
	5% B	0.653	1.000
	10% B	0.629	1.000
Detector 2 1.87 cm Fiber Diameter	PVT	0.509	0.539
	1% B	0.362	0.538
	5% B	0.352	0.539
	10% B	0.336	0.534
Detector 3 1.65 cm Fiber Diameter	PVT	0.395	0.418
	1% B	0.280	0.417
	5% B	0.271	0.415
	10% B	0.265	0.421

The average of each relative response is plotted versus d_{fiber} in Fig. 26. Least squares fitting gave the greatest correlation coefficient ($R^2 = 1$) with a second order polynomial equation. This correlates to the diameter, or radius, squared, which suggests that the relative response between fiber sizes of similar composition is proportional to the difference in fiber volume, as the fiber length was constant.

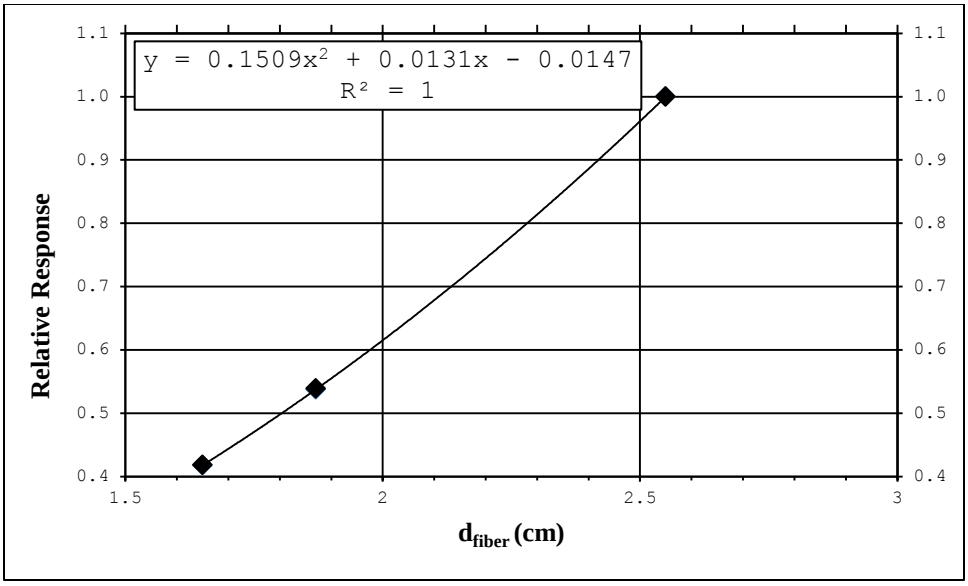

Fig. 26. Average relative response as a function of fiber diameter.

For all fiber diameters, 1% boron loading provides the highest average response of the boron-loaded fibers within all rings, except for the outermost (11") ring of all detectors. The 1% loading of boron (0.1995 % ^{10}B) provides enough target centers to effectively capture thermalized neutrons, while maintaining the highest relative proportion of scintillating material.

3.4 Angular Response

The angular response was examined for the large fiber detector 1 with 1% boron loading, as similar anisotropies were expected for each detector. Detector one was exposed to the same neutron field used previously, at angles of 45° and 90° in the Y-Z plane. As expected, the difference in response between the detector rings becomes negligible as the angle of incidence increased. The response functions for angular response are plotted in Figs. 27 and 28.

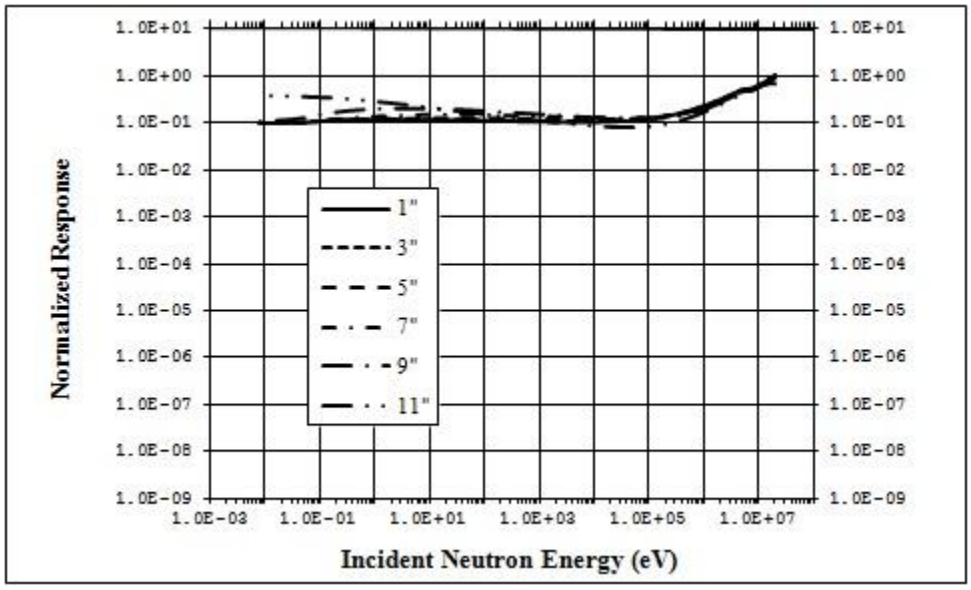

Figure 27. Angular response of detector 1 at 45 degrees.

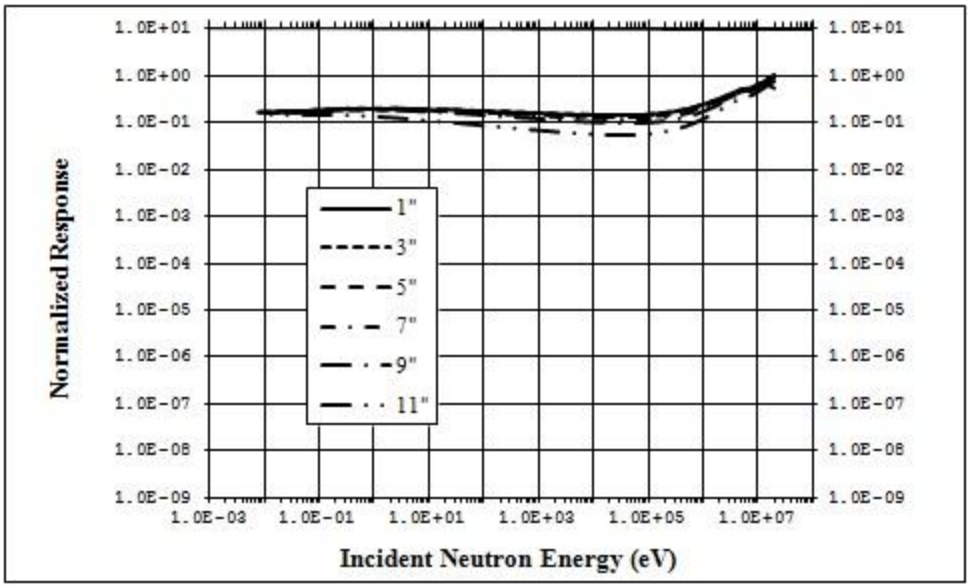

Figure 28. Angular response of detector 1 at 90 degrees.

3.5 Directional and Spectral Information

For each of the simulated detector iterations, spectral fluence information was tallied in each fiber. For example, the multichannel output of a 1% boron-loaded 2.55 cm fiber is provided in Fig. 29. This fiber, taken from the 11" ring of detector one, was simulated with irradiation by 19.95 MeV (Group 1) neutrons. The small peak corresponding to the data point for 1.4609 MeV represents a peak in energy deposition by thermal neutrons in ^{10}B. This peak corresponds to the kinetic energy (1.47 MeV) carried by the α-particle reaction product of the ^{10}B (n, α) ^{7}Li reaction.

Summing the area under this peak with the area under the curve at energies below 1 eV provides an estimate of energy deposition by thermal neutrons. The ratio of this area to the area under the entire curve shows the degree of moderation of the incident neutron field. When plotted with a grey scale for each fiber, as in Fig. 30, the

incident beam direction can be seen. It is clear that as neutrons traverse the detector and are moderated, a higher fraction of energy is deposited within the detector by thermal neutrons.

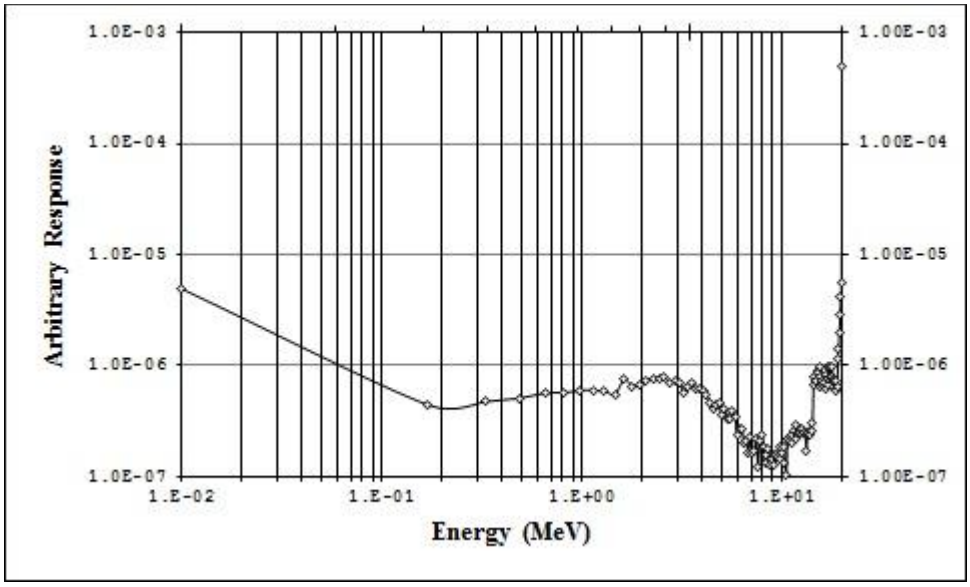

Fig. 29. Multichannel response of a 1% boron-loaded outer fiber of detector 1 when exposed to19.95 MeV (Group 1) neutrons.

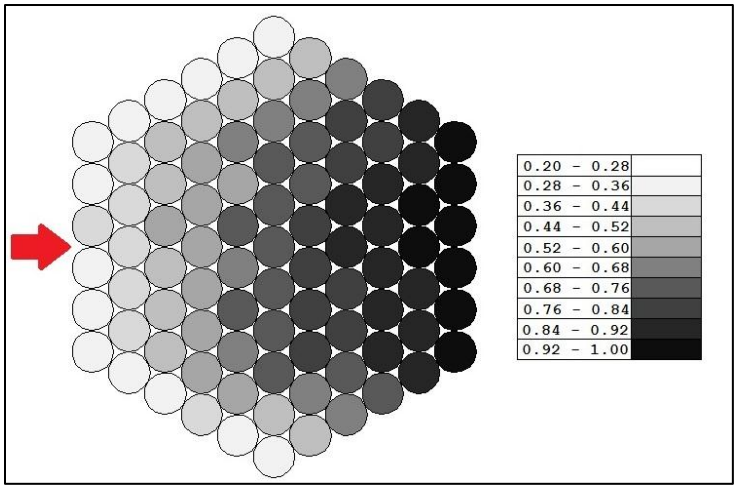

Fig. 30. Directional abilities are shown for a 1% boron-loaded outer fiber of detector 1 when exposed to19.95 MeV (Group 1) neutrons. The red arrow indicates the direction of incident neutrons. The color scale represents the fraction of energy deposition by thermal capture reactions with respect to total energy deposition, normalized to an arbitrary scale.

4. CONCLUSIONS AND RECOMMENDATIONS

4.1 Summary and Conclusions

Hexagonal arrays of plastic scintillation detector fibers show potential for use in neutron spectral measurements. Boron loading increases detector response relative to unloaded plastic at or below neutron energies on the order of 1 MeV. At all but the highest neutron energies, boron-loading does not detract from detector efficiency. Boron loading of 1% natural boron, or 0.9975% ^{10}B, shows the best overall response. Significant loss of differentiation between rings occurs as the angle of incident neutrons increases from the direction normal to the hexagonal array. This may negatively impact detector functionality in some protection scenarios. However, for use in areas where neutron direction can be reasonably assumed, such near accelerator beams, this should not be a detriment. The ability to achieve desired results with only one measurement, as opposed to multiple measurements made with several Bonner spheres, balances anisotropic response. Energy resolution results are equivalent to the energy resolution provided by multi-sphere sets.

The use of solid-state collection and processing electronics, combined with the self-contained nature of the detector system, makes this spectrometer suitable for operational radiological protection use.

4.2 Future Work

The multichannel output of a 1% boron-loaded 2.55 cm fiber in Fig. 29 shows many peaks correlating to proton recoil energy deposition. Proper analysis and calibration will allow neutron spectral information to be obtained from this spectrum. The proton recoil spectra of each fiber may be combined into a new response matrix. The combination of the ring response matrix and the proton recoil response matrix can be used to create a more full response matrix such that less, or no, *a priori* spectral information is needed.

REFERENCES

Alevra AV, Cosack M, Hunt JB, Thomas DJ, Schraube H. Experimental determination of the response of four Bonner sphere sets to monoenergetic neutrons (II). Radiat Prot Dosim 40:91-102; 1992.

Attix FH. Introduction to radiological physics and radiation dosimetry. Weinheim, Germany: WILEY-VCH Verlag GmbH & Co. KGaA; 2004.

Barbagallo M, Cosentino L, Greco G, Guardo G, Montereali RM, Pappalardo A, Scire C, Scire S, Vincenti MA, Finocchiaro P. A thermal neutron mini-detector with SiPM and scintillating fibers. Nucl Instr and Meth 652:355-358; 2011.

Blumenfeld H, Bourdinaud M, Thevenin JC. Plastic fibers in high energy physics. Nucl Instr and Meth 257:603-606; 1987.

Bramblett RL, Ewing RI, Bonner TW. A new type of neutron spectrometer. Nucl Instr and Meth 9:1-12; 1960.

Brooks FD, Klein H. Neutron spectrometry - historical review and present status. Nucl Instr and Meth 476:1-11; 2002.

Caswell RS, Coyne JJ, Randolph ML. Kerma factors for neutron energies below 30 MeV. Rad Res 83:217-254; 1980.

Chadwick J. Possible existence of a neutron. Nature 3252:312; 1932.

Chadwick MB, Hale GM, Young PG, Barschall HH, DeLuca PM, Caswell RS, Jones DTL, MacFarlane RE, Meulders JP, Wambersie A, Schuhmacher H, Schrewe UJ. A consistent set of neutron kerma coefficients from thermal to 150 MeV for biologically important materials. Med Phys 26:974-991; 1999

Chakarova R. Monte carlo study of light transport in scintillating fibers. Nucl Instr and Meth 364:90-94; 1995.

Cruzate JA, Carelli JL, Gregori BN. Bonner sphere spectrometer. In: Workshop on uncertainty assessment in computational dosimetry: a comparison of approaches. Proceedings of an European Radiation Dosimetry Group (EURADOS) conference. Bologna: 2007; 45-52.

Czirr JB, Merrill DB, Beuhler D, McKnight TK, Carroll JL, Abbott T, Wilcox E. Capture-gated neutron spectrometry. Nucl Instr and Meth 476:309-312; 2002.

Drake P, Bartlett DT. Neutron dose equivalent rates calculated from measured neutron angular and energy distributions in working environments. Radiat Prot Dosim 70:235-239; 1997.

Duderstadt JJ, Hamilton LJ. Nuclear reactor analysis. New York, NY: John Wiley & Sons; 1976.

Eichholz GG, Poston JW. Principles of nuclear radiation detection. Ann Arbor, MI: Ann Arbor Science Publishers Inc.; 1982.

El Messaoudi M. Chouak A, Lferde M, Cherkaoui R. Performance of three different unfolding procedures connected to Bonner sphere data. Radiat Prot Dosim 108:247-253; 2004.

Esposito A, Nandy M. Measurement and unfolding of neutron spectra using Bonner spheres. Radiat Prot Dosim 110:555-558; 2004.

Feather N. The collisions of neutrons with nitrogen nuclei. Proc R Soc Lond A 136:709-727; 1932.

Ferrer JC, Carlson JD, Rapaport J. Neutron elastic scattering at 11 MeV and the isospin dependence of the neutron-nucleus optical potential. Nucl Phys A 275:352-341; 1977.

Finocchiaro P, Pappalardo A, Cosentino L, Belluso M, Billotta S, Bonanno G, Carbone B, Condorelli G, Di Mauro S, Fallica G, Mazzillo M, Piazza A, Sanfilippo D, Valvo G. Characterization of a novel 100-channel silicon photomultiplier-part I: noise. IEEE Trans Elec Dev 55:2757-2764; 2008a.

Finocchiaro P, Pappalardo A, Cosentino L, Belluso M, Billotta S, Bonanno G, Carbone B, Condorelli G, Di Mauro S, Fallica G, Mazzillo M, Piazza A, Sanfilippo D, Valvo G. Characterization of a novel 100-channel silicon photomultiplier-part II: charge and time. IEEE Trans Elec Dev 55:2765-2773; 2008b.

Finocchiaro P, Pappalardo A, Cosentino L, Belluso M, Billota S, Bonanno G, Di Mauro S. Features of silicon photo multipliers: precision measurements of noise, cross-talk, afterpulsing, detection efficiency. IEEE Trans Nucl Sci 56:1033-1041; 2009.

Firk FWK. Neutron time-of-flight spectrometers. Nucl Instr and Meth 162:539-563; 1979.

Fowler JL, Brolley JE. Monoenergetic neutron techniques in the 10 to 30 MeV range. Reviews of Modern Physics, 28:103-134; 1956.

Freeman DW, Edwards DR, Bolon AE. Genetic algorithms - a new technique for solving the neutron spectrum unfolding problem. Nucl Instr and Meth 425:549-576; 1999.

Garcia-Dominguez E. Vega-Carillo HR, de Leon GM, McBride LE. Noniterative unfolding algorithm for neutron spectrum measurements with Bonner spheres. IEEE Transactions on Nuclear Science 46:28-35; 1999.

Goldhagen P, Reginatto M, Kniss T, Wilson JW, Singleterry RC, Jones IW, Van Steveninck W. Measurement of the energy spectrum of cosmic-ray induced neutrons aboard an ER-2 high-altitude airplane. Nucl Instr and Meth 476:42-51; 2002.

Grazioso RF, Heger AS, Ensslin N, Mayo DR, Mercer DJ, Miller MC, Russo PA. Feasibility of using boron-loaded plastics for neutron detection. Nucl Instr and Meth 422:59-63; 1999.

International Atomic Energy Agency. Compendium of neutron spectra and detector responses for radiation protection purposes. Supplement to Technical Reports Series No. 318. Vienna, Austria: IAEA; IAEA Technical Reports Series No. 403; 2001.

International Commission on Radiological Protection. 1990 Recommendations of the International Commission on Radiological Protection. Oxford, UK: Pergamon Press; ICRP Publication 60; Ann ICRP 21(1/3); 1991.

International Commission on Radiological Protection. The 2007 Recommendations of the International Commission on Radiological Protection. Oxford, UK: Pergamon Press; ICRP Publication 103; Ann ICRP 37(2/4); 2007.

Karim A, Arendt BH, Goyette R, Huang YY, Kleb R, Felcher GP. An automated neutron reflectometer (POSY II) at the intense pulsed neutron source. Physica B 173:17-24; 1991.

Klein H. Workplace radiation field analysis. Radiat Prot Dosim 70:225-234; 1997.

Klykov SA, Ul'yanenko SE, Matusevich ES, Kurachenko YA, Dulin VA. Tissue absorbed dose from a gadolinium layer irradiated with neutrons. Atomic Energy 96:430-433; 2004

Knoll GF. Radiation detection and measurement, 3rd ed. New York, NY: John Wiley & Sons; 2000.

Kralik M, Aroua A, Grecescu M, Mares V, Novotny T, Schraube H, Wiegel B. Specification of Bonner sphere systems for neutron spectrometry. Radiat Prot Dosim 70:279-284; 1997.

Kuijpers L, Herzing R, Cloth P, Filges D, Hecker R. On the determination of fast neutron spectra with activation techniques; its application in a fusion reactor blanket model. Nucl Instr and Meth 144:215-224; 1977.

Lacoste V, Gressier V, Pochat JL, Fernandez F, Bakali M, Bouassoule T. Characterization of Bonner sphere systems at monoenergetic and thermal neutron fields. Radiat Prot Dosim 110:529-532; 2004.

Lide DR, Alberty RA, Berger LI, Covington AK, Fischer K, Fontaine JC, Fuhr JR, Gmehling J, Goldberg RN, Holden NE, Kehiaian HV, Kerr JA, Krafczyk J, Lovas FJ, Luo YR, Martin WC, Menke J, Miller TM, Mohr PJ, Powell CJ, Reader J, Redhead PA, Snyder LE, Taylor BN, Vanysek P, Wiese WL, Wohlfarth C, Zwillinger D, Zyla P. CRC handbook of chemistry and physics, 86th ed. Boca Raton, Florida: CRC Press; 2005.

Loong CK, Ikeda S, Carpenter JM. The resolution function of a pulsed-neutron chopper spectrometer. Nucl Instr and Meth 260:381-402; 1987.

Mares V, Schraube H. Evaluation of the response matrix of a Bonner sphere spectrometer with LiI detector from thermal energy to 100 MeV. Nucl Instr and Meth 337:461-473; 1994.

Mares V, Schraube G, Schraube H. Calculated neutron response of a Bonner sphere spectrometer with He-3 counter. Nucl Instr and Meth 307:398-412; 1991.

Matzke M. Propagation of uncertainties in unfolding procedures. Nucl Instr and Meth 476:230-241; 2002.

Matzke M, Kluge H, Luszik-Bhadra M. Directional information on neutron fields. Radiat Prot Dosim 70:261-264; 1997.

Moody KJ, Hutcheon ID, Grant PM. Nuclear forensic analysis. Boca Raton, FL: CRC Press; 2005.

Mukherjee B. A high-resolution neutron spectra unfolding method using the genetic algorithm technique. Nucl Instr and Meth 476:247-251; 2002.

Naismith OF, Siebert BRL. A database of neutron spectra, instrument response functions, and dosimetric conversion factors for radiation protection applications. Radiat Prot Dosim 70:241-245; 1997.

Naismith OF, Siebert BRL, Thomas DJ. Response of neutron dosimeters in radiation protection environments: an investigation of techniques to improve estimates of dose equivalent. Radiat Prot Dosim 70:55-260; 1997.

Nanstad RK, Farrell K, Braski DN, Corwin WR. Accelerated neutron embrittlement of ferritic steels at low fluence: flux and spectrum effects. J Nucl Mat 158:1-6; 1988.

National Nuclear Data Center [database online]. Upton, New York: Brookhaven National Laboratory; 2011. Updated December 2011.

Peel J, Mascarenhas N, Mengesha W, Sunnarborg D. Development of a directional scintillating fiber detector for 14 MeV neutrons. Nucl Instr and Meth 556:287-290; 2006.

Pichenot G, Guldbakke S, Asselineau B, Gressier V, Itie C, Klein H, Knauf K, Lebreton L, Lob S, Pochon-Guerin L, Schlegel D, Sosaat W. Characterisation of spherical recoil proton proportional counters used for neutron spectrometry. Nucl Instr and Meth 476:165-169; 2002.

Reginatto M, Goldhagen P, Neumann S. Spectrum unfolding, sensitivity analysis and propagation of uncertainties with the maximum entropy deconvolution code MAXED. Nucl Instr and Meth 476:242-246; 2002.

Routti JT, Sandberg JV. Unfolding activation and multisphere detector data. Radiat Prot Dosim 10:103-110; 1985.

Sawan M, Conn RW. Neutron pulses slowing down in heavy media: analysis with applications of the lead spectrometer. Nucl Sci Eng 54:127-142; 1974.

Shultis JK, Faw RE. An MCNP primer. 2006.

Singkarat S, Garis NS, Grosshog G. The feasibility of using plastic scintillation fibers for fast neutron spectrometry. Nucl Instr and Meth 335:248-254; 1993.

Singkarat S, Boonyawan D, Hoyes GG, Tippawan U, Vilaithong T, Garis NS, Kobus H. Development of an encapsulated scintillating fiber detector as a 14-MeV neutron sensor. Nucl Instr and Meth 384:463-470; 1997.

Stacey WM. Nuclear reactor physics. Weinheim, Germany: WILEY-VCH Verlag GmbH & Co. KGaA; 2004.

Takasaki F, Saito H, Shimizu T, Kondo S, Shinji O. Development of plastic scintillation fiber. Nucl Instr and Meth 262:224-228; 1987.

Tang S, Ma Q, Yin Z, Huang H. Determination of spatial resolution of plastic scintillation fiber array with a simple method. Nuclear Science and Techniques 18:111-114; 2007.

Telling MTF, Andersen KH. Spectroscopic characteristics of the OSIRIS near-backscattering crystal analyser spectrometer on the ISIS pulsed neutron source. Phys Chem Chem Phys 7:1255-1261; 2005.

Thomas DJ. Neutron spectrometry. Radiat Meas 45:1178-1185; 2010.

Thomas DJ, Alevra AV. Bonner sphere spectrometers - a critical review. Nucl Instr and Meth 476:12-20; 2002.

Thomas DJ, Alevra AV, Hunt JB, Schraube H. Experimental determination of the response of four Bonner sphere sets to thermal neutrons. Radiat Prot Dosim 54:25-31; 1994.

Thomas DJ, Bardell AG, Macaulay EM. Characterization of a gold foil-based Bonner sphere set and measurements of neutron spectra at a medical accelerator. Nucl Instr and Meth 476:31-35; 2002.

Titt U, Breskin A, Chechik R, Dangendorf V, Grosswendt B, Schuhmacher H. Concept of a neutron dosimeter based on a recoil particle track chamber. Radiat Prot Dosim 70:219-224; 1997.

Tosi G, Torresin A, Agosteo S, Foglio Para A, Sangiust V, Zeni L. Neutron measurements around medical electron accelerators by active and passive detection techniques. Med Phys 18:54-60; 1991.

Tsoulfanidis N. Measurement and detection of radiation, 2nd ed. Washington, DC: Taylor & Francis; 1983.

Turner JE. Atoms, radiation, and radiation protection, 3rd ed. Weinheim, Germany: WILEY-VCH Verlag GmbH & Co. KGaA; 2007.

Twomey S. On the numerical solution of fredholm integral equations of the first kind by the inversion of the linear system produced by quadrature. JACM 10:97-101; 1963.

Vivani M, Kievsky A, Girlanda L, Marucci LE, Rosati S. Neutron-triton elastic scattering. Few-body Systems 45:119-121; 2009.

Vylet V. Response matrix of an extended Bonner sphere system. Nucl Instr and Meth 476:26-30; 2002.

Wiegel B. Alevra AV. NEMUS - the PTB neutron multisphere spectrometer: Bonner spheres and more. Nucl Instr and Meth 476:36-41; 2002.

Yan X, Titt U, Koehler AM, Newhauser WD. Measurement of neutron dose equivalent to proton therapy patients outside of the proton radiation field. Nucl Instr and Meth 476:429-434; 2002.

Zhang Q, Wang Q, Xie Z, Niu S. Study on the energy response to neutrons for a new scintillating-fiber-array neutron detector. Nucl Instr and Meth 496:146-153; 2003.

Zheng Y, Fontenot J, Taddei P, Mirkovic D, Newhauser W. Monte carlo simulations of neutron spectral fluence, radiation weighting factor and ambient dose equivalent for a passively scattered proton therapy unit. Phys Med Biol 53:187-201; 2008.

APPENDIX A

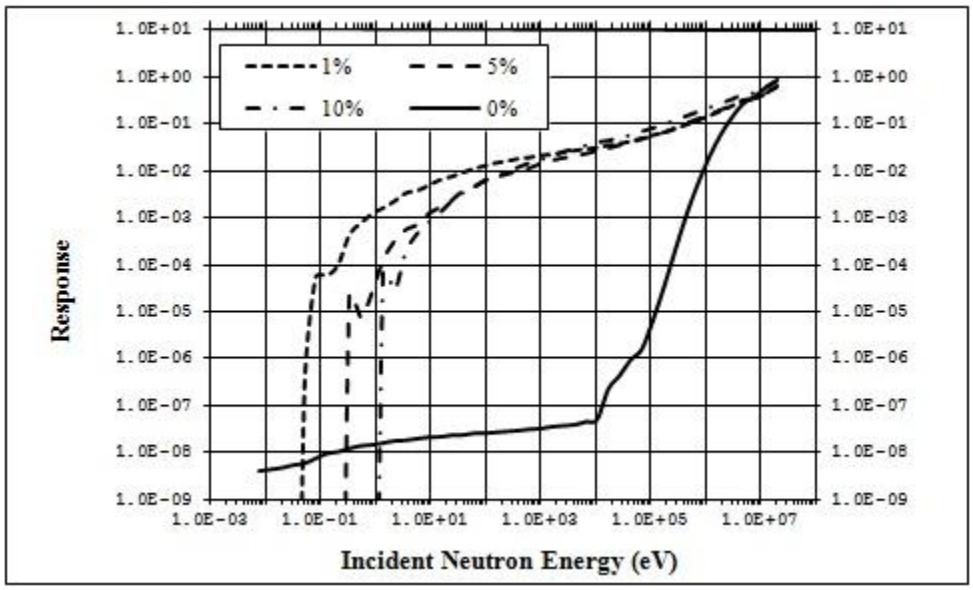

Fig. A1. Response functions are shown for the four material compositions for the 1" ring of detector 1 (large fiber).

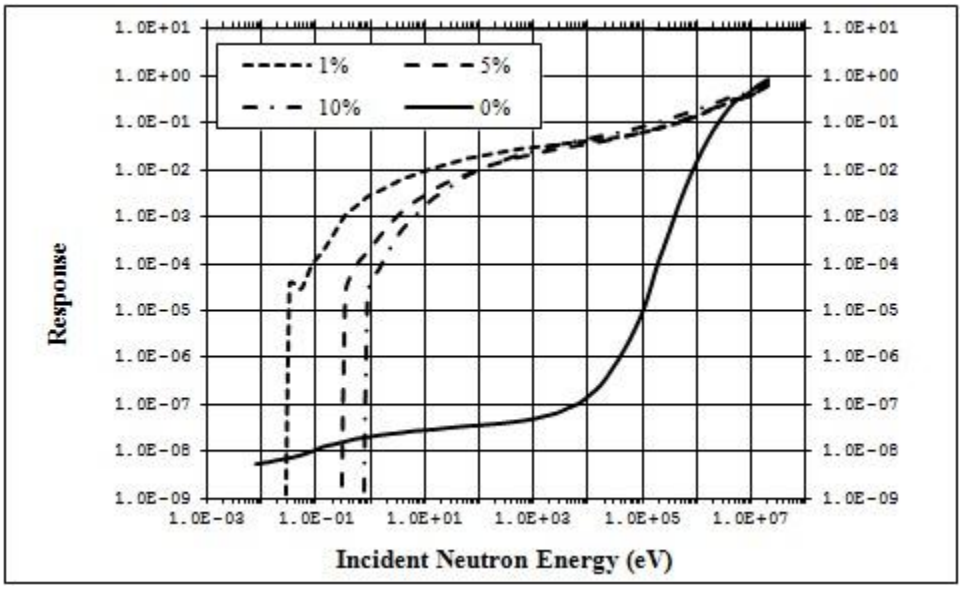

Fig. A2. Response functions are shown for the four material compositions for the 3" ring of detector 1 (large fiber).

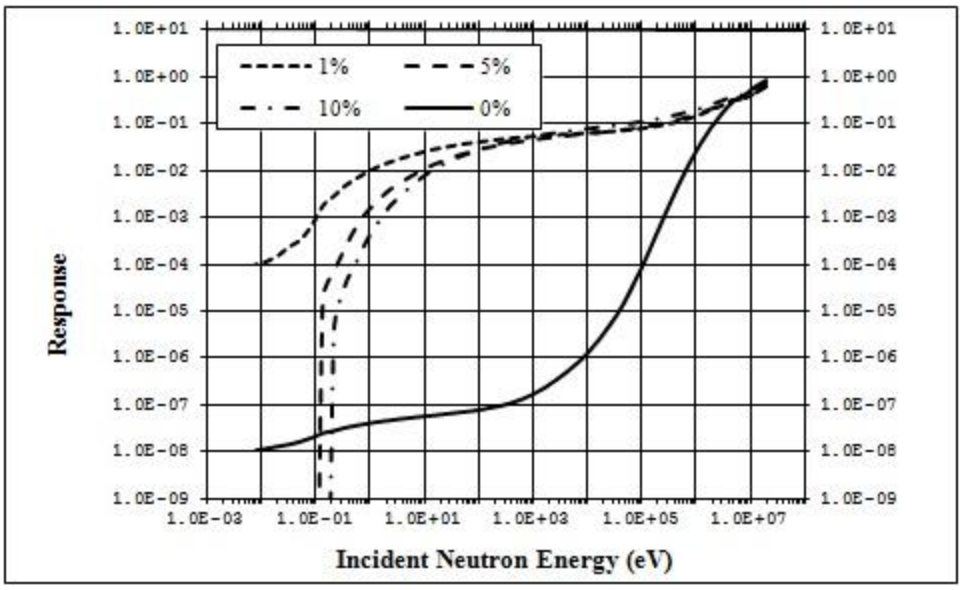

Fig. A3. Response functions are shown for the four material compositions for the 5" ring of detector 1 (large fiber).

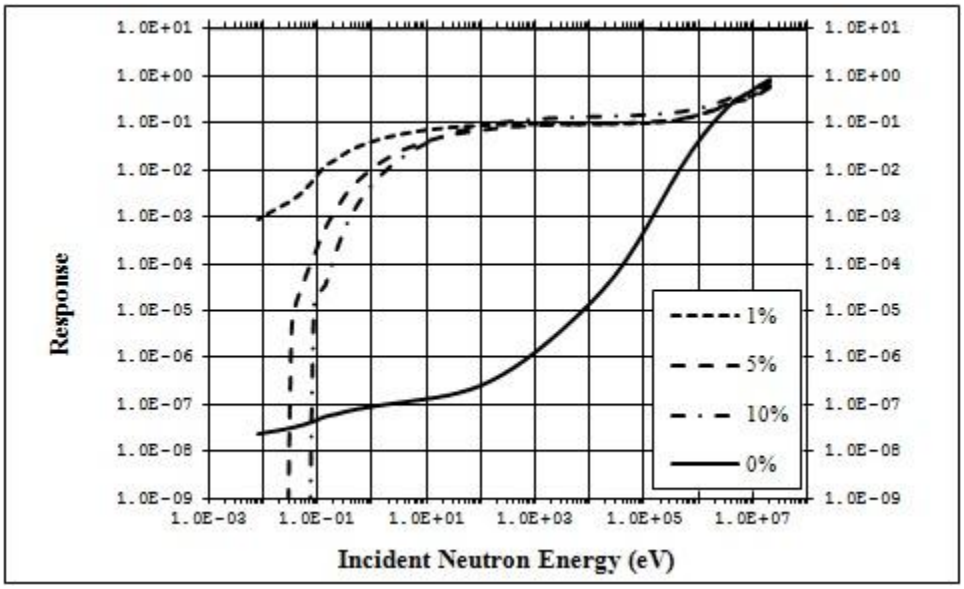

Fig. A4. Response functions are shown for the four material compositions for the 7" ring of detector 1 (large fiber).

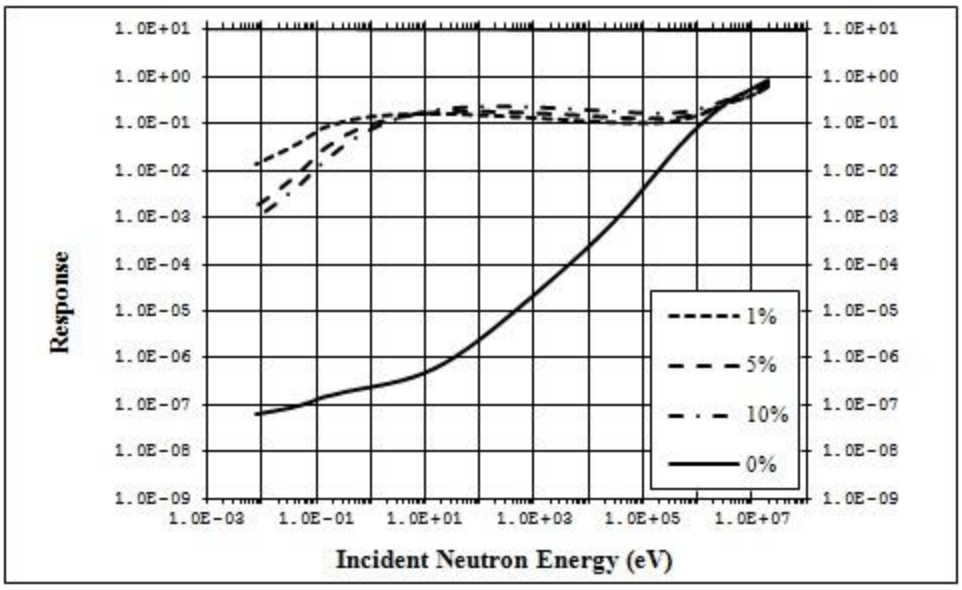

Fig. A5. Response functions are shown for the four material compositions for the 9" ring of detector 1 (large fiber).

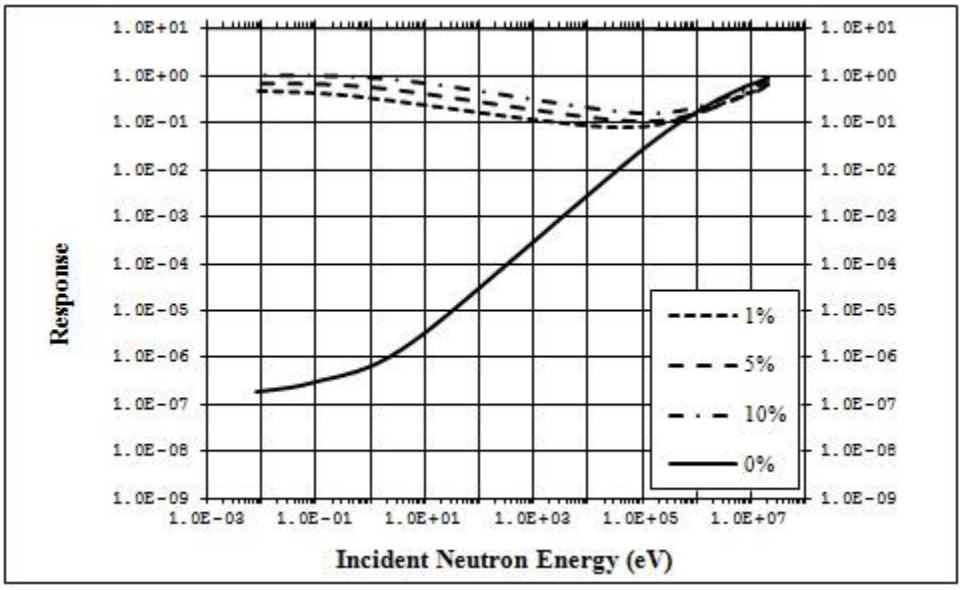

Fig. A6. Response functions are shown for the four material compositions for the 11" ring of detector 1 (large fiber).

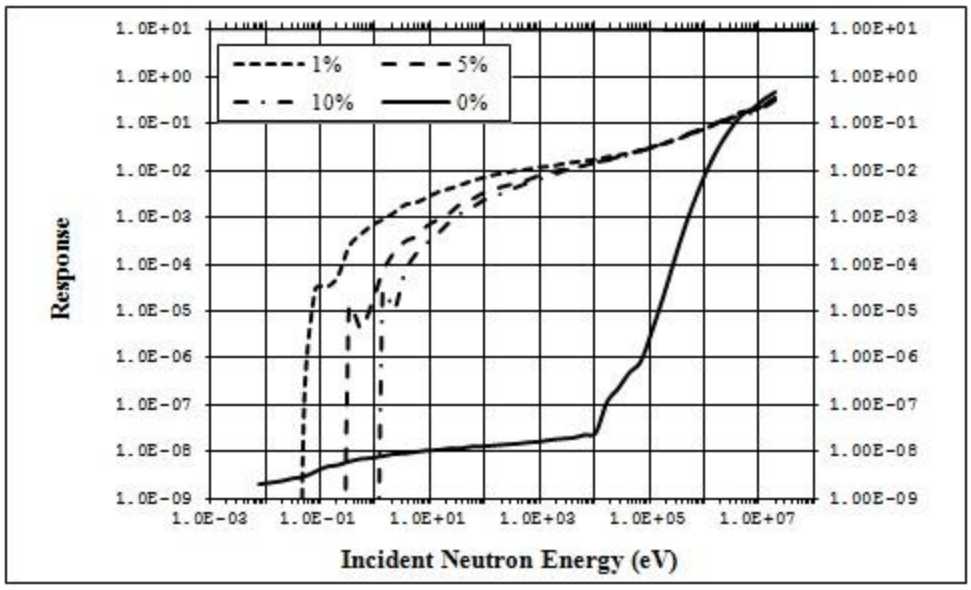

Fig. A7. Response functions are shown for the four material compositions for the 1" ring of detector 2 (medium fiber).

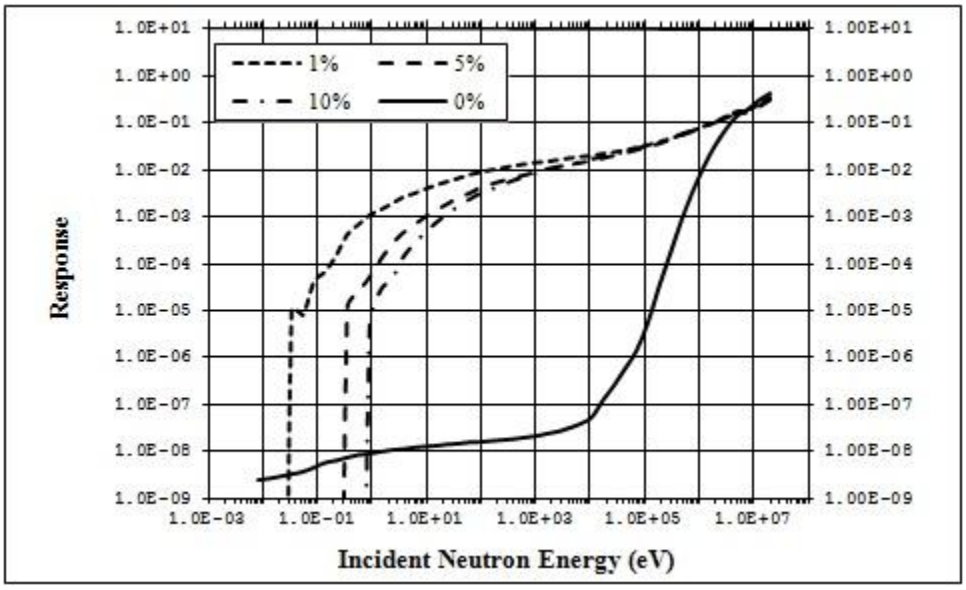

Fig. A8. Response functions are shown for the four material compositions for the 2" ring of detector 2 (medium fiber).

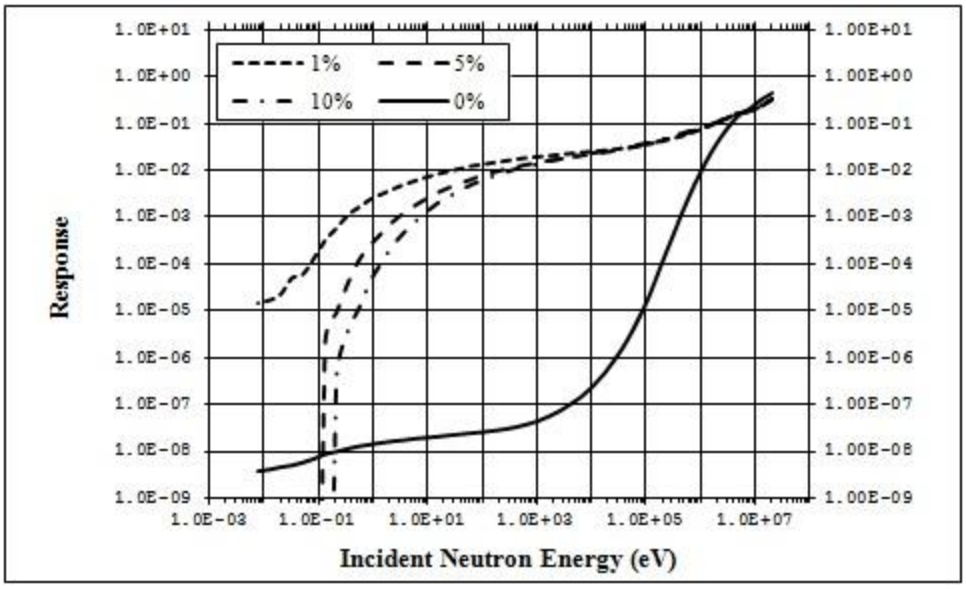

Fig. A9. Response functions are shown for the four material compositions for the 3.5" ring of detector 2 (medium fiber).

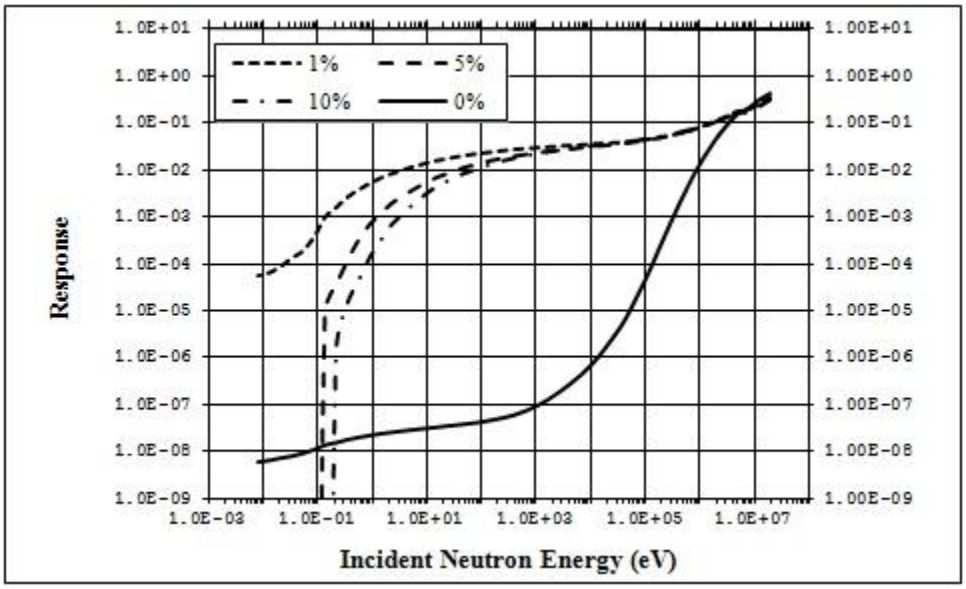

Fig. A10. Response functions are shown for the four material compositions for the 5" ring of detector 2 (medium fiber).

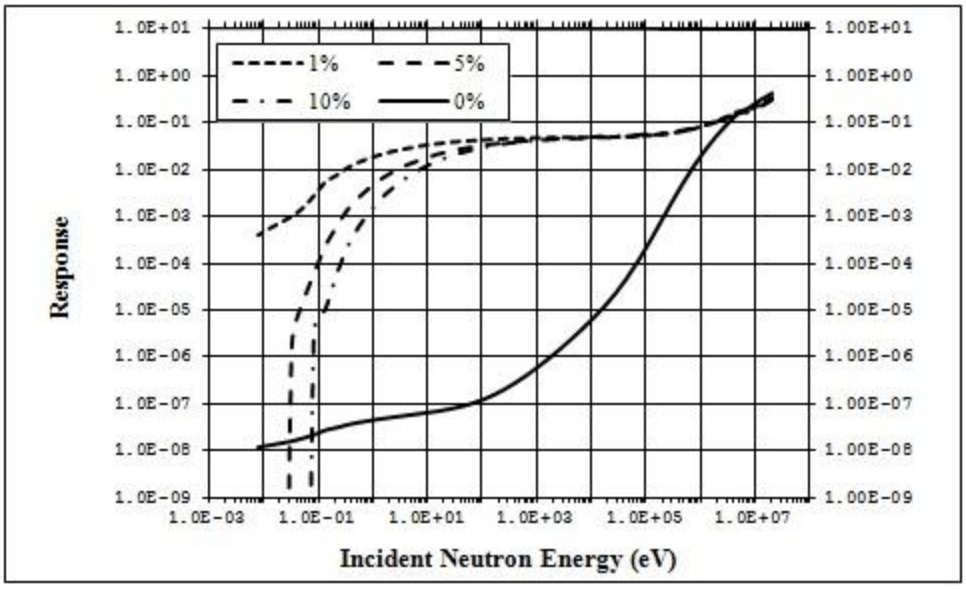

Fig. A10. Response functions are shown for the four material compositions for the 6.5" ring of detector 2 (medium fiber).

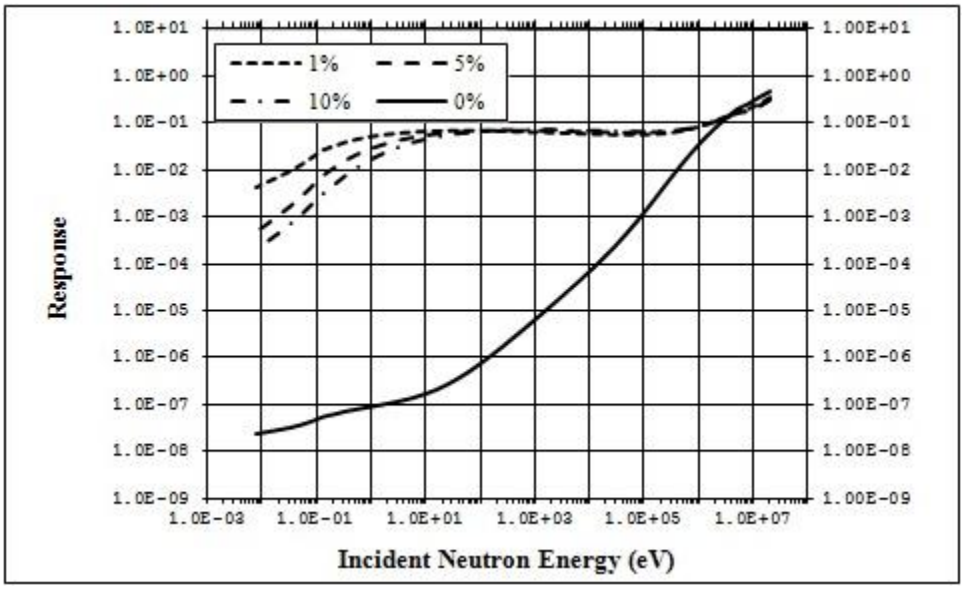

Fig. A12. Response functions are shown for the four material compositions for the 8" ring of detector 2 (medium fiber).

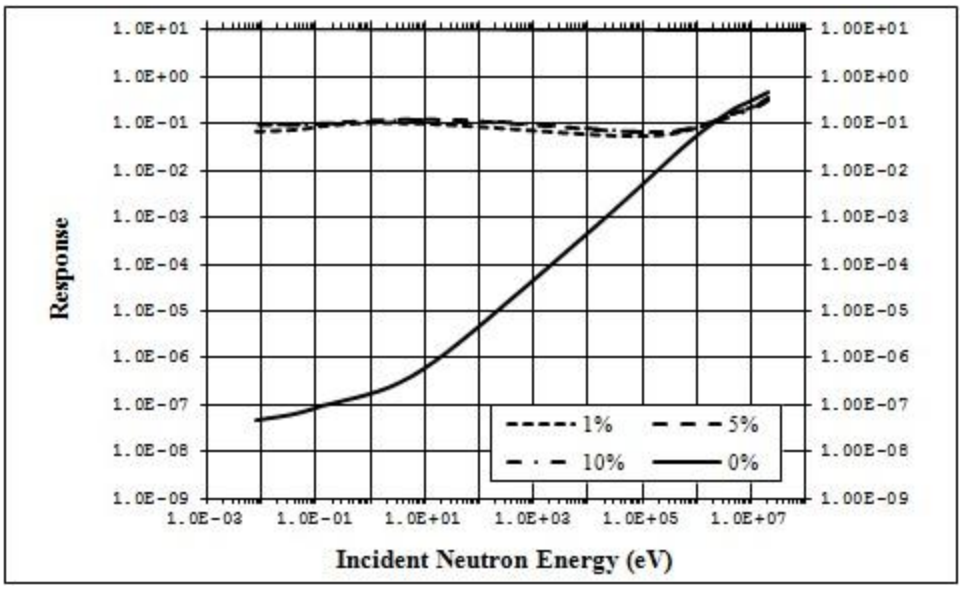

Fig. A13. Response functions are shown for the four material compositions for the 9.5" ring of detector 2 (medium fiber).

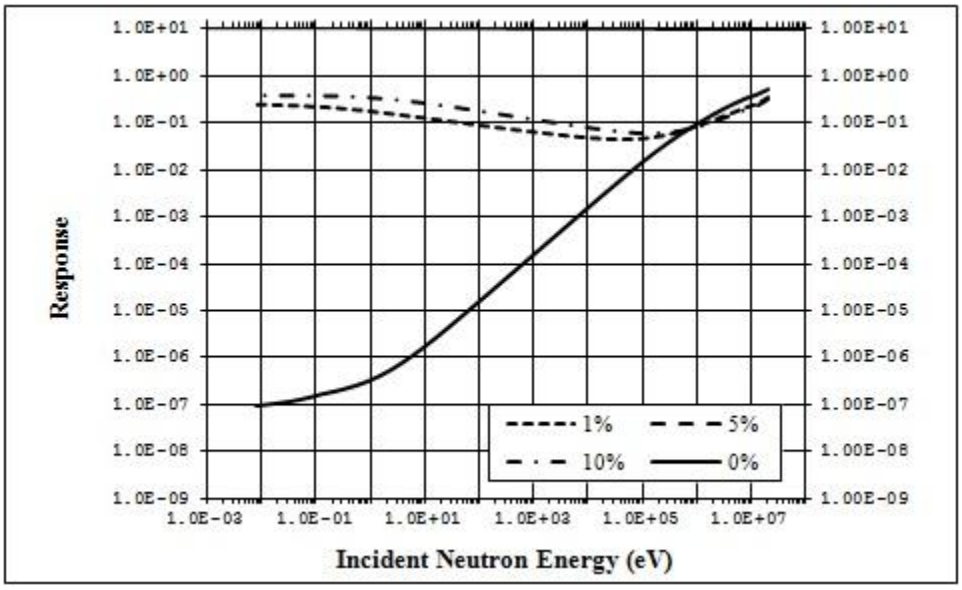

Fig. A14. Response functions are shown for the four material compositions for the 11" ring of detector 2 (medium fiber).

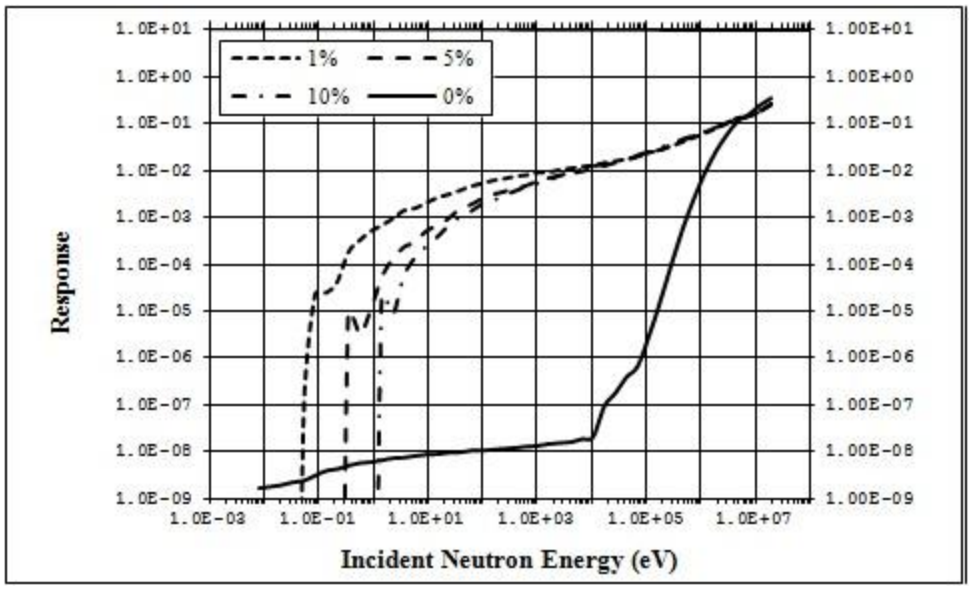

Fig. A15. Response functions are shown for the four material compositions for the 0.5" ring of detector 3 (small fiber).

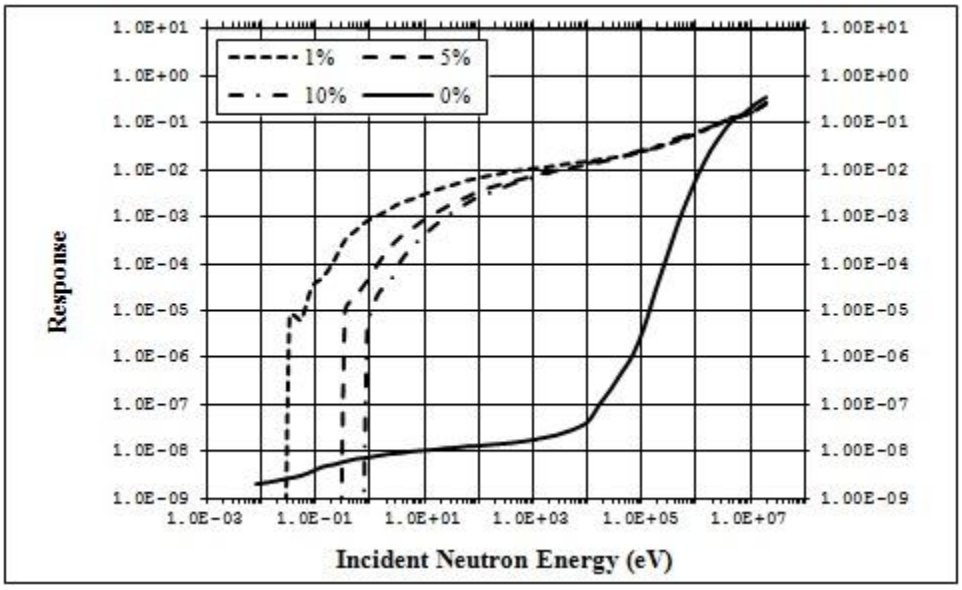

Fig. A16. Response functions are shown for the four material compositions for the 2" ring of detector 3 (small fiber).

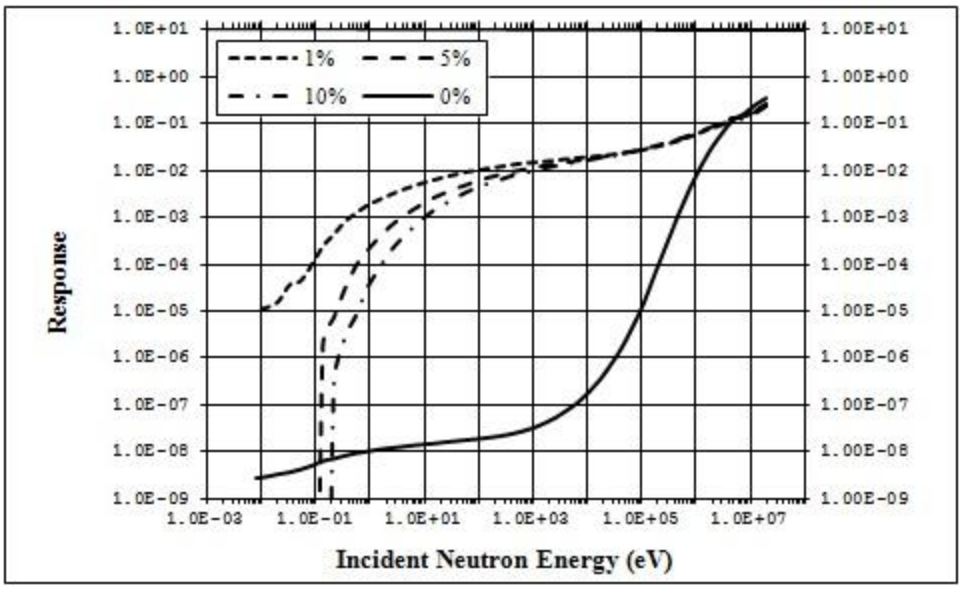

Fig. A17. Response functions are shown for the four material compositions for the 3" ring of detector 3 (small fiber).

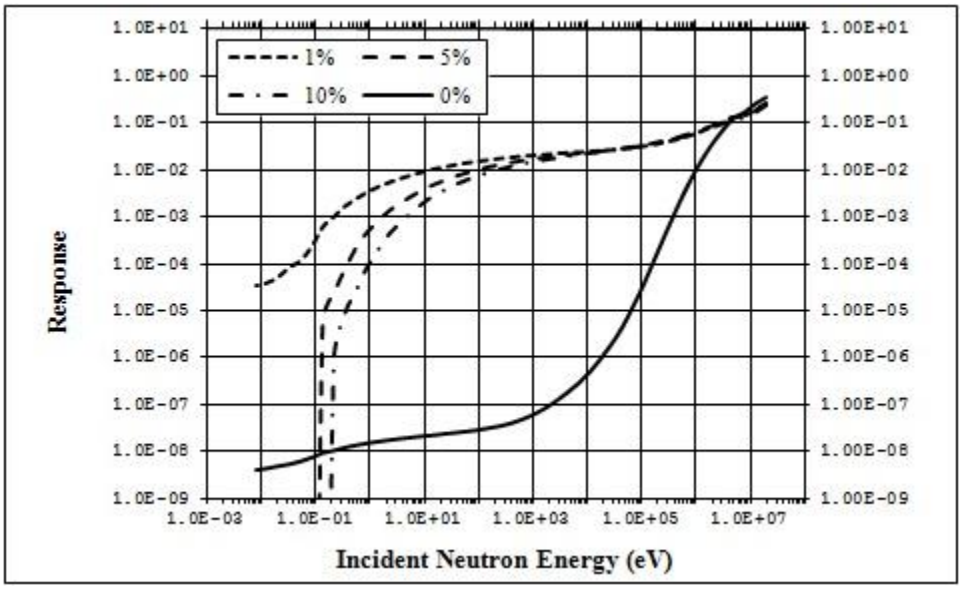

Fig. A18. Response functions are shown for the four material compositions for the 4.5" ring of detector 3 (small fiber).

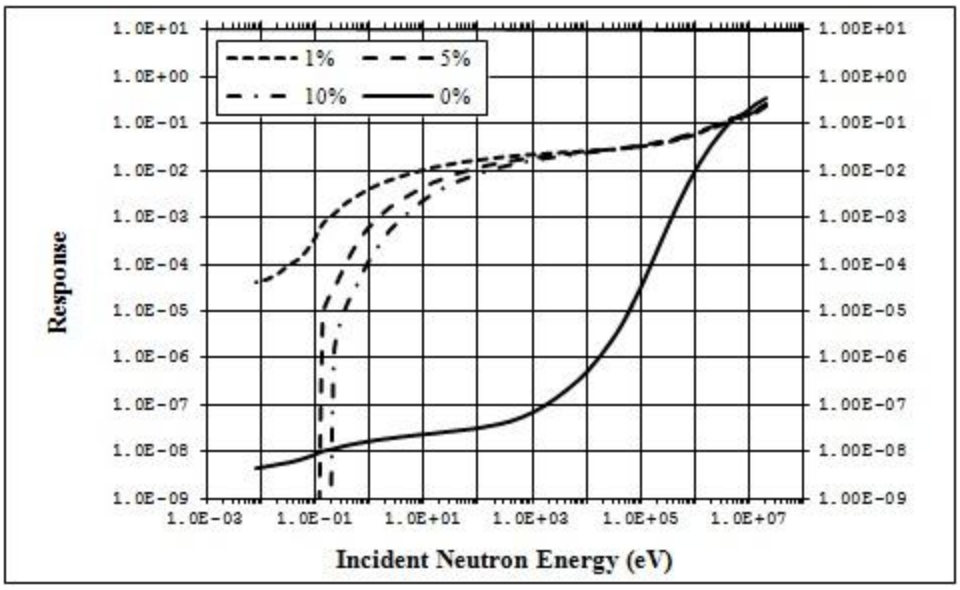

Fig. A19. Response functions are shown for the four material compositions for the 6" ring of detector 3 (small fiber).

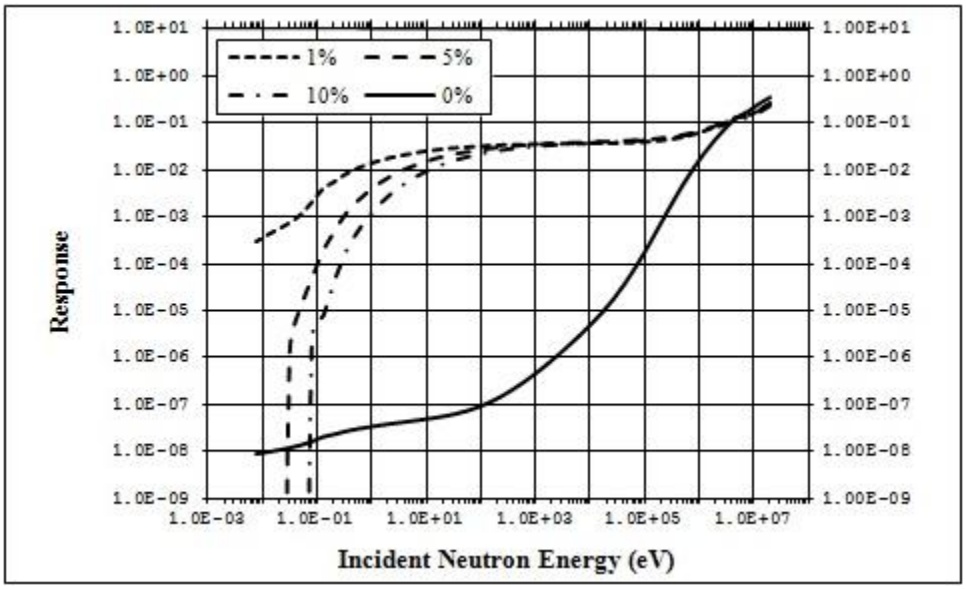

Fig. A20. Response functions are shown for the four material compositions for the 7" ring of detector 3 (small fiber).

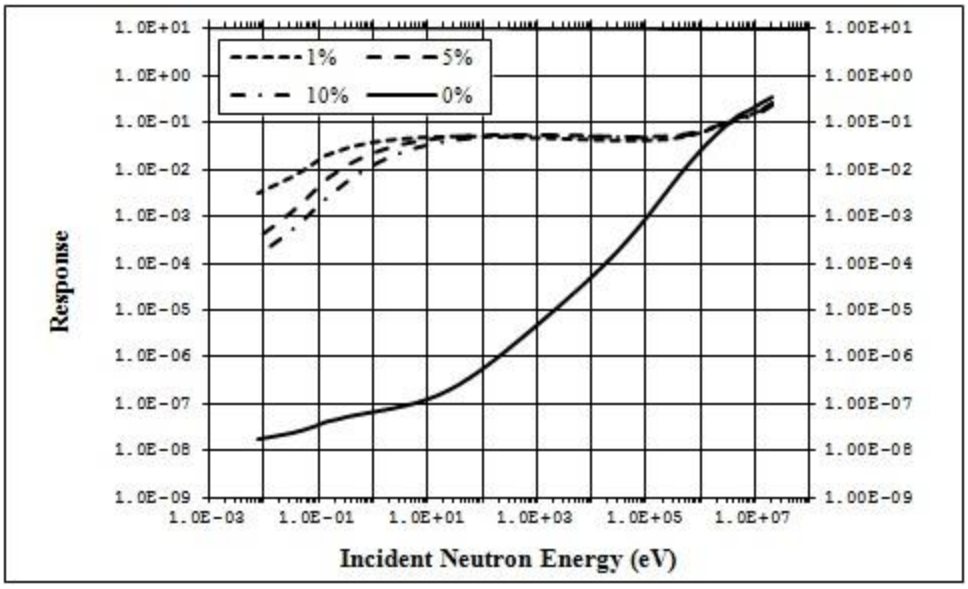

Fig. A21. Response functions are shown for the four material compositions for the 8.5" ring of detector 3 (small fiber).

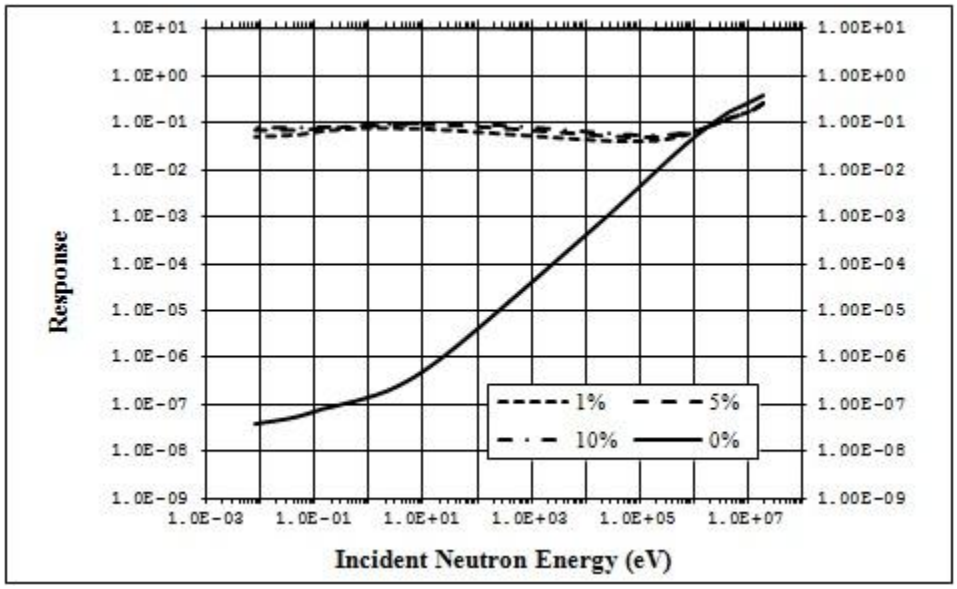

Fig. A22. Response functions are shown for the four material compositions for the 9.5" ring of detector 3 (small fiber).

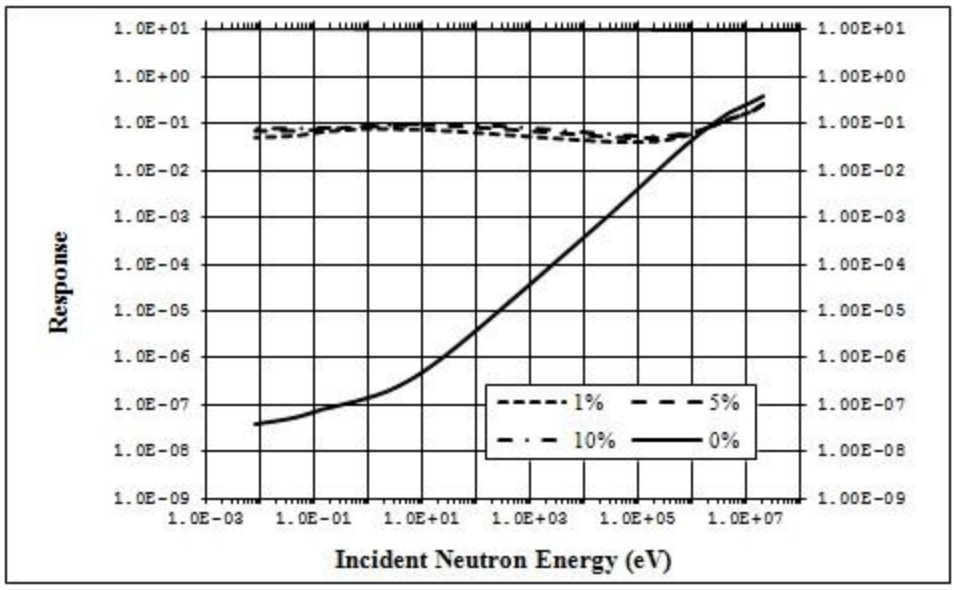

Fig. A23. Response functions are shown for the four material compositions for the 11" ring of detector 3 (small fiber).

VITA

Name:	Thomas Michael Martin
Address:	337 Zachry Engineering Center 3133 TAMU College Station, TX 77843-3133
Email Address:	tmichaelmartin@tamu.edu
Education:	M.S., Health Physics, Texas A&M University, 2012 B.S., Nuclear Engineering, Texas A&M University, 2009